

# Electrochemically Engineered Lanthanum Nickelate as a Promising Transparent Hole-Transport Layer for Bulk Heterojunction Polymer Solar Cells: An Experimental and DFT Study

Shirzad Jouybar, Leila Najji,\* Sayed Ahmad Mozaffari, Saeedeh Sarabadani Tafreshi,\* and Nora H. de Leeuw



Cite This: <https://doi.org/10.1021/acsaem.3c03274>



Read Online

ACCESS |



Metrics & More



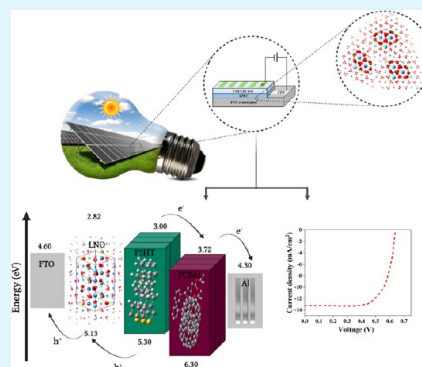
Article Recommendations



Supporting Information

**ABSTRACT:** Lanthanum nickelate (LNO) was grown on an FTO-coated glass slide by employing the chronoamperometry method and used as a hole transport layer (HTL) in bulk heterojunction polymer solar cells (BHJ PSCs). The electrodeposition parameters, including the deposition time, potential magnitude, and electrolyte conditions, were changed to obtain LNO thin films, providing appropriate energy levels as an HTL. The electrochemical, morphological, optical, and structural characteristics of electrochemically produced LNO samples were compared to those of the sample prepared via the sol–gel procedure. The LNO sample prepared by applying  $-1.18$  V while the electrolyte was stirring exhibited significantly better electrochemical and optical properties. The fabricated PSC using this sample provided a considerably higher (45.3%) power conversion efficiency (PCE) than the PSC prepared based on an LNO thin film acquired by the sol–gel method. The superior performance of the BHJ PSC was ascribed to the increased electroactive surface area ( $1.341$  cm<sup>2</sup>), improved charge mobility ( $2.30 \times 10^{-6}$  cm<sup>2</sup> V<sup>-1</sup> s<sup>-1</sup>), and reduced charge recombination probabilities. A short circuit current of  $13.24$  mA cm<sup>-2</sup>, an open circuit voltage of approximately  $0.64$  V, a fill factor of 70%, an external quantum efficiency of 75.3%, and a PCE of 5.9% were demonstrated by the best fabricated PSC, surpassing the reference device with a PEDOT:PSS HTL. Moreover, the prepared PSC exhibited remarkable ambient stability, maintaining 84% of its initial PCE after 450 h of aging. The agreement between DFT calculations and experimental results confirmed that LNO possesses the optical and elastic characteristics required to improve the efficiency and stability of PSCs as an HTL.

**KEYWORDS:** polymer solar cell, hole transporting layer, electrodeposition, perovskite oxide (LaNiO<sub>3</sub>), DFT calculations



## 1. INTRODUCTION

Perovskite oxides are a class of ternary metal oxides with the general formula ABO<sub>3</sub>, where A is a cation with a larger atomic radius from alkaline earth or rare-earth metals and B is a smaller cation from transition metals (e.g., Ni, Co, Ti, Mn, and Fe).<sup>1</sup> The smaller cation B is situated inside the oxygen octahedra, interconnected by corner-sharing. Conversely, the larger cation A is coordinated with 12 oxygen anions at the dodecahedral positions.<sup>2</sup> These compounds have received a lot of attention due to their special features, such as structural flexibility, fascinating electrocatalytic and thermodynamic characteristics, stability, low toxicity, and various synthesis methods.<sup>3</sup> The characteristics of oxides in general and perovskite oxides in particular are tightly related to their lattice structure; breaking the lattice symmetry can significantly alter the characteristics of these materials.<sup>4</sup> Ideal perovskite oxides have a highly symmetric cubic lattice that may undergo distortion and convert into less symmetric structures of tetragonal, monoclinic, orthorhombic, triclinic, and rhombohedral.<sup>5</sup> The perovskites' dielectric, magnetic, optical, and

catalytic characteristics may be governed by the tilted and rotated oxygen octahedra.<sup>2</sup> Perovskite oxide compounds show metallic, semiconductive, and insulating properties, depending on the type and size of metals in their structures.<sup>4</sup> Due to their diverse compositions and features, perovskite oxides have become extremely important and have been extensively used in various fields, including water splitting, fuel cells, photocatalysis, light-emitting diodes, electrochemical devices, and solar energy conversion.<sup>6</sup> Different perovskite oxides could be easily synthesized using a variety of techniques, including sol–gel, co-precipitation, solid-state, hydrothermal, self-assembly, and template approaches.<sup>7</sup> The applied synthesis method could significantly affect the crystallinity, morphology, particle

**Received:** December 30, 2023

**Accepted:** January 29, 2024

dimension, and specific surface area of the synthesized perovskite oxides, which consequently could influence the application of these compounds in different areas.<sup>8</sup> In recent years, some perovskite oxides, such as BaSnO<sub>3</sub> and SrTiO<sub>3</sub>, BaTiO<sub>3</sub> with semiconductor characteristics have been applied as the charge-transporting layer (CTL) in perovskite solar cells (Per-SCs), which has enhanced their efficiency.<sup>9</sup> Also, an increasing number of investigations have been conducted on using La<sub>1-x</sub>Ce<sub>x</sub>NiO<sub>3</sub>, La<sub>1-x</sub>Ca<sub>x</sub>MnO<sub>3</sub> as counter electrodes and CdSnO<sub>3</sub>, BaSnO<sub>3</sub>, BaTiO<sub>3</sub>, and SrTiO<sub>3</sub> as the working electrode in the fabrication of dye-synthesized solar cells (DSSCs), resulting in an improvement in their performance.<sup>10</sup> In comparison, the number of studies on the application of these materials in polymer solar cells (PSCs) is considerably limited.

The CTLs, that is, the hole transporting layer (HTL) and electron transporting layer (ETL), are used between the electrodes and photoactive layer in PSCs and Per-SCs to tune work functions and energy levels, form an ohmic contact, diminish the energy barrier, improve charge selectivity, and increase charge collection efficiencies of holes and electrons by anode and cathode electrodes, respectively.<sup>11</sup> Moreover, the structural, optical, and electrochemical properties of CTLs can considerably impact the performance of PSCs and Per-SCs.<sup>11</sup> Notably, various materials have been employed as an ETL for high-performance PSCs, while the development of HTLs lags significantly behind.<sup>12</sup> The most commonly used materials as ETL are LiF, ZnO, TiO<sub>2</sub>, and PFN.<sup>13</sup> Due to its unique properties, including transparency, mechanical permanence, solution processability, and compatibility with various photoactive layers, polyethylenedioxythiophene:polystyrenesulfate (PEDOT:PSS) has been employed as the HTL in the majority of reported high-performance PSCs.<sup>14</sup> However, some main disadvantages of PEDOT:PSS, such as an acidic and hydrophilic nature, inadequate electron-blocking potential, and heterogeneous electrical features, cause conventional PSCs to have short lifetimes and a low power conversion efficiency (PCE) and also experience quick degradation.<sup>15</sup> In order to avoid the drawbacks of PEDOT:PSS, considerable endeavors have been dedicated to the advancement of alternative HTLs, including metal oxides such as V<sub>2</sub>O<sub>5</sub>, MoO<sub>3</sub>, WO<sub>3</sub>, NiO<sub>x</sub>, CrO<sub>x</sub>, and CuO<sub>x</sub>, polymers, carbon nanotubes, graphene oxide, and reduced graphene oxide.<sup>16,17</sup>

Due to the high stability and low cost of binary metal oxides, they have drawn much interest and have been extensively studied as an HTL in PSCs. However, their fixed characteristics, such as band gaps, energy levels, transmittance, conductivity, and so on, are their primary limitations as HTLs.<sup>18</sup> Because of the varying energy levels of donor and acceptor compounds employed in the photoactive layer, these fixed characters of binary metal oxides restrict the flexibility of PSCs in general applications. To conquer these weak points while maintaining the advantages of utilizing metal oxides as HTLs, the design of ternary metal oxides, such as perovskite oxides with tunable physicochemical properties and band structure, can be a critical approach to promoting PSC performance.<sup>19</sup>

Lanthanum nickelate (LaNiO<sub>3</sub>, LNO) is one of the perovskite oxide materials that has attained considerable attention because of its exceptional features, including thermal stability, high conductivity, thermoelectric and catalytic activity.<sup>20</sup> LNO has found a wide range of applications, including ferroelectrics, dielectrics, conductive thin films,

therapeutics, and photocatalysis.<sup>21</sup> Compared to other perovskite oxides such as SrTiO<sub>3</sub>, BaSnO<sub>3</sub>, BaTiO<sub>3</sub>, and so on, fewer investigations have reported the application of LNO in the fabrication of solar cells. Nevertheless, experimental and theoretical studies on the LNO have revealed that this compound can be used as a CTL in the construction of solar cells.<sup>20,21</sup> In the sole study published on the utilization of LNO as HTL in PSCs, a sample of this compound with a band gap of 3.45 eV and transparency of >80% was prepared by the sol-gel procedure. The PCE of 9.45% has been recorded in this work by employing the PTB7-Th:PC71BM active layer.<sup>20</sup> Preparing homogeneous thin layers to construct PSCs has always been a significant challenge in solar cell design.<sup>22</sup> Since the ultimate performance of the PSCs can be remarkably influenced by the structural characteristics of its constituent layers, developing these devices and enhancing their efficiency via the implementation of single-step, repeatable, and cost-effective procedures could be highly beneficial.

Electrodeposition (ED) is an adaptable method for fabricating thin films that has many advantages over more traditional methods like physical vapor deposition (PVD), sputtering, chemical vapor deposition (CVD), and pulsed laser deposition (PLD). These advantages include implementation simplicity, minimal material and energy consumption, low temperature, affordability, scalability, and nontoxicity.<sup>23</sup> The electrodeposited thin film characteristics are highly affected by the ED potential, precursor salt concentrations, deposition time, temperature, and rate of electrolyte stirring.<sup>24</sup> The ED approach has already been utilized to synthesize several metal oxides such as V<sub>2</sub>O<sub>5</sub>, NiO, ZnO, and so on by investigating parameters such as the electrolyte concentration and comparing different ED techniques such as cyclic voltammetry (CV), chronoamperometry (CA), chronopotentiometry (CP), and so on. The findings revealed that by adjusting the indicated parameters and changing the physical and electrochemical properties of the produced nanomaterials, the photovoltaic performance of PSCs could be improved.<sup>16,17</sup>

Researchers have recently conducted extensive experimental and computational studies using different device structures, compositions, and fabrication methods to improve the stability and efficiency of PSCs.<sup>25</sup> Computational chemistry, which has developed into a new tool for scientific investigation, can simulate several screening experiments, which could considerably accelerate this research.<sup>26</sup> Motivated by the high interest in fully exploiting the potential of LNO as a CTL in the PSC structure, we present a combined experimental and computational study to discover how LNO might increase the efficiency and stability of PSC. According to most recent findings, perovskite oxides have not yet been synthesized by the ED method to be utilized in the fabrication of all kinds of solar cells. In the current work, LNO nanostructures were electrochemically produced on the FTO-coated glass slide via the CA method. Several synthetic parameters, such as the ED time, electrolyte stirring, and ED potential, were altered to achieve the optimal ED state. Physical and electrochemical evaluation of the acquired LNO thin films by ED was performed. The results were compared with each other and with those obtained utilizing the sol-gel procedure and spin-coated on the transparent FTO photoanode. Based on the obtained results, the prepared samples were suitable to be employed as an HTL in the construction of BHJ PSC with P3HT:PCBM as the active layer. Then, the performance characterization was carried out on the fabricated PSCs. The

results revealed that the PSC manufactured utilizing LNO prepared under stirring and a cathodic potential of  $-1.18$  V provided superior performance. In order to provide a more precise comparison and validate the experimental results, computational calculations were employed on the rhombohedral LNO, taking into account the X-ray diffraction data that revealed that rhombohedral LNO is synthesized during the ED process. DFT calculations, a commonly used theoretical method for comprehending the properties of diverse materials, were employed to determine the optical absorption coefficient, reflectivity, and elastic characteristics of rhombohedral LNO. Eventually, based on the experimental findings confirmed by computational results, the employment of LNO as HTL could enhance the efficiency and stability of the PSCs.

## 2. EXPERIMENTAL DETAILS

**2.1. Chemicals.** The main reagents used in this work are listed in the Supporting Information (Text S1).

**2.2. Electrochemical Deposition of the LNO Thin Film.** The electrochemical procedure was performed to synthesize LNO nanostructures by co-depositing  $\text{La}(\text{OH})_3$  and  $\text{Ni}(\text{OH})_2$  through nitrate reduction. In order to co-deposit  $\text{La}(\text{OH})_3$  and  $\text{Ni}(\text{OH})_2$  in a 1:1 ratio, 25 mL of an aqueous solution containing  $\text{La}(\text{NO}_3)_3 \cdot 6\text{H}_2\text{O}$  (10 mM),  $\text{Ni}(\text{OH})_2 \cdot 4\text{H}_2\text{O}$  (9 mM), and  $\text{KNO}_3$  (200 mM) was utilized as the electrolyte solution. During the ED process, a single-compartment cell was used with three electrodes. The working electrode was made of an FTO-coated glass slide, the counter electrode was a platinum rod, and the reference electrode was composed of a saturated Ag/AgCl electrode. In order to perform the ED process, the FTO-coated glass slides were first separated into smaller dimensions of 1.5 cm  $\times$  1.5 cm. The slides were then subjected to a series of treatments to eliminate any contaminants that may affect the accuracy of the results. Specifically, the slides underwent etching in a solution composed of HCl,  $\text{H}_2\text{O}$ , and  $\text{HNO}_3$  (24:24:2 v/v). Subsequently, the slides were subjected to sonication in acetone and isopropanol for 15 min each. After each step, the slides were carefully washed with DI water to remove any remaining impurities. Following washing, the FTO slides were dried in an oven at 120 °C for 15 min and then employed as the working electrode. The ED was conducted potentiostatically by applying  $-1.18$  V to the FTO vs Ag/AgCl at an ambient temperature.<sup>27</sup> In order to acquire the desired thin film of LNO nanostructures, the potentiostatic ED procedure was performed at three deposition times of 1, 2, and 4 min by employing a cathodic potential of  $-1.18$  V to the working electrode. The prepared samples in this step were named LNO-TF/ED-T1, LNO-TF/ED-T2, and LNO-TF/ED-T4 to indicate the ED duration.

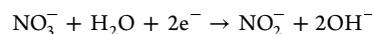
In the next step, the impact of solution stirring on the quality and features of the resulting thin film was explored. The ED of the LNO was performed by applying a potential of  $-1.18$  V at the optimal time of 2 min (based on the physicochemical and electrochemical results), whereas the electrolyte solution was gently stirred utilizing a magnetic stirrer at the speed of 100 r.p.m. The obtained sample in this stage was named LNO-TF/ED-V1.

Eventually, the optimal ED potential was determined by precisely repeating the ED procedure at two other potentials of  $-1.13$  and  $-1.09$  V while the solution was stirred slowly for 2 min as in the previous step at a speed of 100 rpm. The obtained samples using  $-1.13$  and  $-1.09$  V were designated as LNO-TF/ED-V2 and LNO-TF/ED-V3, respectively.

After rinsing with DI water, all samples were transferred to a furnace for annealing. Perovskite oxides are fully crystalline at 550 °C, and the ideal temperature for crystallization is typically between 600 and 900 °C.<sup>20</sup> However, it was discovered that the FTO transparent conductive electrode loses conductivity when subjected to high temperatures ( $>600$  °C) during thermal annealing. Therefore, the annealing process was performed for 5 h at the highest temperature of 600 °C that can be tolerated by FTO.

Considering that the X-ray diffraction (XRD) pattern of the FTO substrate can interfere with the diffraction pattern of the LNO film, a platinum plate was employed as the working electrode while the counter and reference electrodes remained constant. The ED process was performed by employing a potential of  $-1.18$  V for 120 min. As previously performed in some other studies, this step was undertaken to ensure that any interference caused by the FTO substrate was eliminated and that a clear diffraction pattern of the LNO film could be obtained for an accurate comparison with the powder sample acquired via the sol-gel procedure.<sup>20</sup>

In the above-explained ED process, a rise in the local pH can occur at the surface of the working electrode once a potential is given to the electrode to convert nitrate into nitrite in an aqueous solution.



Consequently, the solubilities of  $\text{La}^{3+}$  and  $\text{Ni}^{2+}$  on the electrode surface diminish, and these ions can be precipitated as  $\text{La}(\text{OH})_3$  and  $\text{Ni}(\text{OH})_2$ , respectively.<sup>27</sup> The as-deposited mixed metal hydroxide film on the platinum surface was rinsed with DI water, dried at room temperature, and put in the furnace for annealing. The annealing process was performed at 600 °C for 5 h. The obtained black film was scratched from the platinum surface and used for characterization. The prepared sample was named LNO-P/ED-600.

**2.3. Sol-Gel Synthesis of LNO.** A solution of  $\text{La}(\text{NO}_3)_3 \cdot 6\text{H}_2\text{O}$  (10 mM),  $\text{Ni}(\text{OH})_2 \cdot 4\text{H}_2\text{O}$  (10 mM), and  $(\text{C}_6\text{H}_8\text{O}_7 \cdot \text{H}_2\text{O})$  (50 mM) was prepared in 100 mL of DI water. This solution became pretty transparent after adding a small amount of liquid ammonia to control the pH to 7. In order to initiate the dehydration process, the solution was heated to 130 °C on a hot plate for 2 h with constant stirring. Polycondensation of citric acid and nitrates occurred during the dehydration process.<sup>28</sup> A small amount of the obtained transparent viscous solution in this phase was used to prepare the LNO thin film by a spin-coating technique. First, a layer of the indicated solution was spin-coated on the FTO substrate with a rotation speed of 3000 rpm for 1 min. The deposited FTO was left in an oven to be dried at 85 °C for 10 min.<sup>20</sup> These processes were carried out seven times to ensure that the entire surface was covered and to produce the desired thickness of the thin layer. Subsequently, the deposited film was postannealed in a furnace at 600 °C for 5 h. The prepared sample was named LNO-TF/SG. The remaining part of the transparent viscous solution was annealed at 600 °C for 5 h. The obtained powder sample was named LNO-P/SG-600 and used for further characterization. The names of all the prepared samples under different conditions are listed in Table S1.

**2.4. Characterization of the LNO Nanostructures.** The main methods and the details for the physicochemical and electrochemical characterization of LNO nanostructures in this work are described in Texts S2 and S3.

**2.5. Construction of BHJ PSC Devices.** Considering the physicochemical and electrochemical evaluation, the prepared LNO samples were appropriate to be applied as HTL in the structure of PSC. Therefore, following the provided instructions, conventional PSCs were fabricated with the FTO/LNO/P3HT:PCBM/Al structure. A solution of P3HT:PCBM (1:1, 10 mg/mL in chlorobenzene) was stirred for 12 h and then sonicated at room temperature for 15 min. A spin-coating technique was employed to deposit 150  $\mu\text{L}$  of the prepared active layer solution onto the LNO-coated FTO substrate at 1500 rpm. Finally, the cathode electrode consisting of a thin layer of Al (200 nm) was deposited onto the prepared films utilizing the PVD technique. To compare the photovoltaic characteristics of the LNO-based solar cell with the reference solar cell made of the PEDOT:PSS, a solution containing 5 mg of this compound was added to 5 mL of DI water. This solution was then spin-coated onto the FTO electrode at 2000 rpm. The active layer solution was also prepared using the same method and spin-coated onto the electrode that had already been coated with the PEDOT:PSS layer. Finally, a 100 nm-thick aluminum cathode was deposited on the electrode by employing the PVD technique. All of the described procedures were performed in a glovebox filled with  $\text{N}_2$ . The fabricated cells based on LNO and PEDOT:PSS thin films as

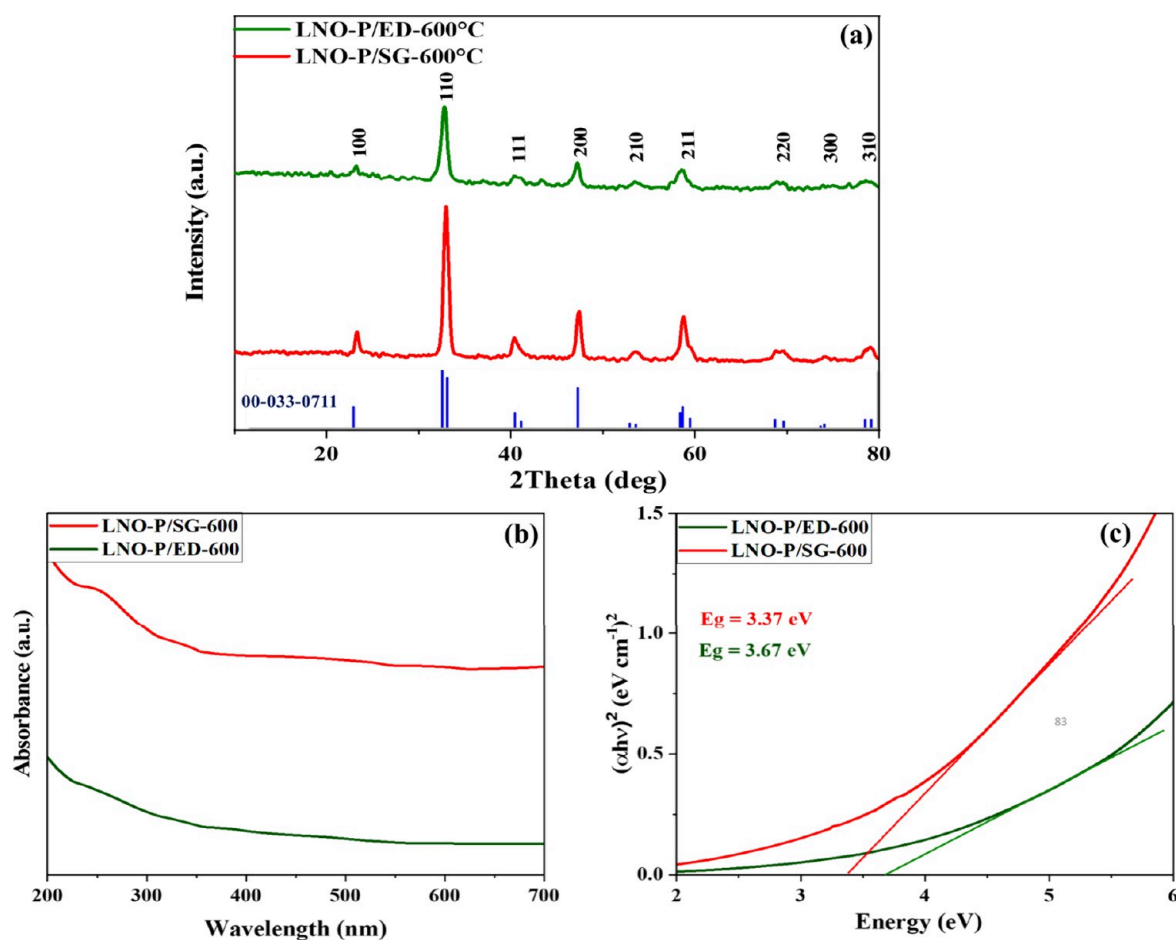


**Figure 1.** (a) XRD patterns, (b) UV–vis absorption spectra of the LNO suspension dispersed in  $\text{H}_2\text{O}:\text{C}_2\text{H}_5\text{OH}$  (1:1 v/v) with a concentration of  $\sim 0.2$  mM, and (c) the corresponding Tauc's plots of the synthesized LNO by the sol–gel (LNO-P/SG-600) and ED (LNO-P/ED-600) methods.

HTL were named PSC-LNO-TF/ED-T2, PSC-LNO-TF/ED-V1, PSC-LNO-TF/ED-V2, PSC-LNO-TF/ED-V3, PSC-LNO-SG, and PSC-PEDOT:PSS. The name and constituent parts of the fabricated PSCs are listed in Table S2.

During the Al deposition process, a shadow mask consisting of six identical windows was used to ensure uniform active area for all fabricated PSCs. The evaluation of the current density–voltage ( $J$ – $V$ ) characteristics for the developed cells was conducted utilizing a Zive SPI Potentiostat/Galvanostat while subjecting them to AM 1.5 illumination at an intensity of  $100 \text{ mW cm}^{-2}$ . The Enli Technology Company's QE-R solar cell spectrum response evaluation system was used to determine the external quantum efficiency (EQE) of the produced PSCs throughout the wavelength range of 300 to 800 nm.

**2.6. Computational Method.** The details for density functional theory (DFT) calculation used in this work is explained in Text S4 (Supporting Information).

### 3. RESULTS AND DISCUSSION

**3.1. Structural and Morphological Analysis of the Synthesized Samples.** The crystallinity and phase purity of the LNO powder samples synthesized using the sol–gel (LNO-P/SG-600) and ED (LNO-P/ED-600) methods were investigated utilizing XRD spectroscopy. The XRD spectra of the LNO samples after calcination at  $600^\circ\text{C}$  are represented in Figure 1a. To verify that the crystallization of the LNO nanostructures was completed at  $600^\circ\text{C}$ , the annealing process of samples acquired by sol–gel and ED procedures was also carried out for 5 h at  $800^\circ\text{C}$ . The XRD patterns of LNO-P/SG-800 and LNO-P/ED-800 samples are depicted in Figure

S2. The presence of LNO crystals was verified in both cases by the detection of characteristic diffraction peaks located at  $2\theta = 23.21^\circ, 32.86^\circ, 40.71^\circ, 47.30^\circ, 53.50^\circ, 58.64^\circ, 69.06^\circ, 73.95^\circ,$  and  $78.4^\circ$  related to (100), (110), (111), (200), (210), (211), (220), (300), and (310) planes, respectively. As illustrated in Figure 1a and Figure S2, the XRD patterns of all samples are well matched with those of the JCPDS card no. (00-033-0711) labeled as  $\text{LaNiO}_3$  with a rhombohedral crystalline structure, and no peaks related to other materials such as  $\text{La}_2\text{O}_3$  or NiO were observed.<sup>28</sup> As depicted in Figure S2, the diffraction peak intensity increased by increasing the calcination temperature for samples obtained from the sol–gel and ED methods. The average crystallite size of LNO nanoparticles synthesized by the sol–gel method and calcinated at two different temperatures of  $600^\circ\text{C}$  (88.6 nm) and  $800^\circ\text{C}$  (167.0 nm) was compared with those provided by the ED method at  $600^\circ\text{C}$  (30.83 nm) and  $800^\circ\text{C}$  (134.1 nm). The results revealed that higher calcination temperatures led to larger crystallite sizes.<sup>29</sup> Additionally, the nanoparticles produced by the sol–gel approach were found to be larger than those produced by the ED method at both calcination temperatures. Fundamentally, the nucleation and growth processes govern the production of nanoparticles in a reaction.<sup>30,31</sup> Results suggest that the nucleation rate in the ED approach is greater than that of the sol–gel method, resulting in the formation of a smaller crystallite size of LNO, which is probably due to a lower growth rate.

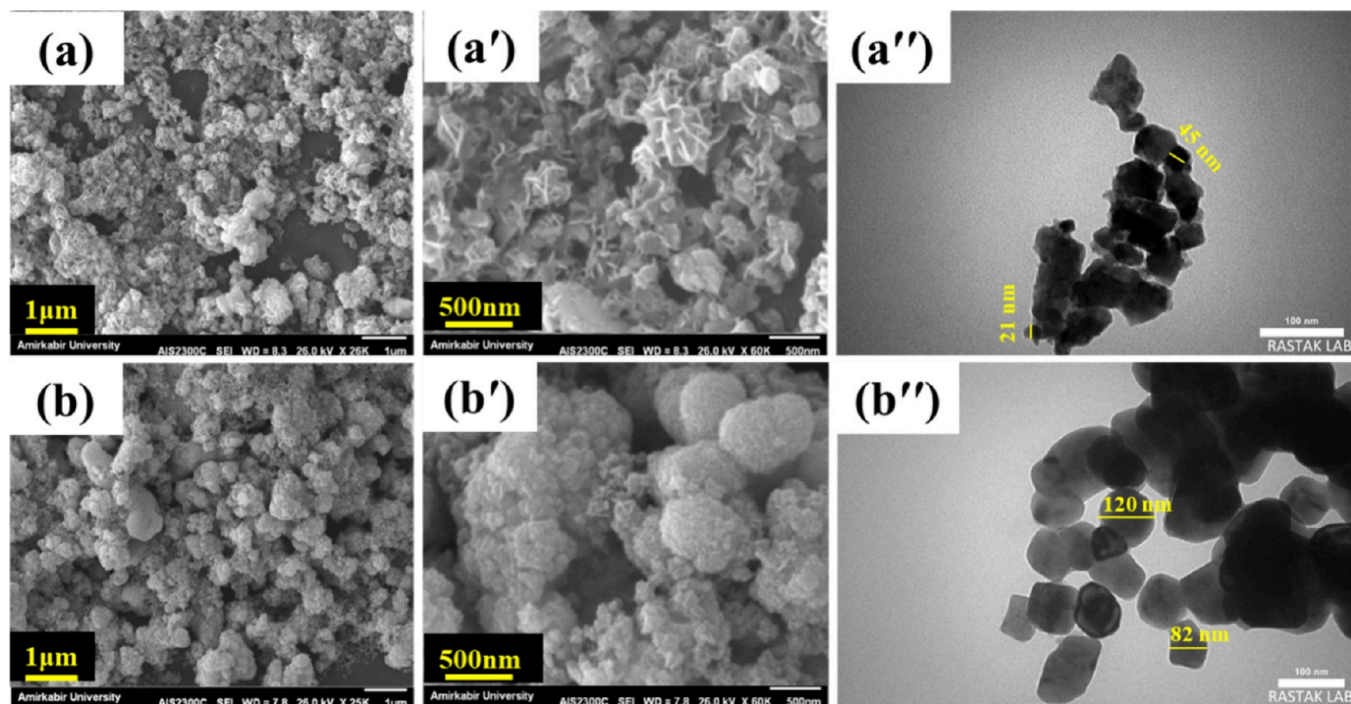


**Figure 2.** SEM images of (a, a') LNO-P/ED-600 and (b, b') LNO-P/SG-600 and (a'') corresponding TEM images of synthesized LNO powders by the ED (LNO-P/ED-600) and (b'') sol-gel (LNO-P/SG-600) methods.

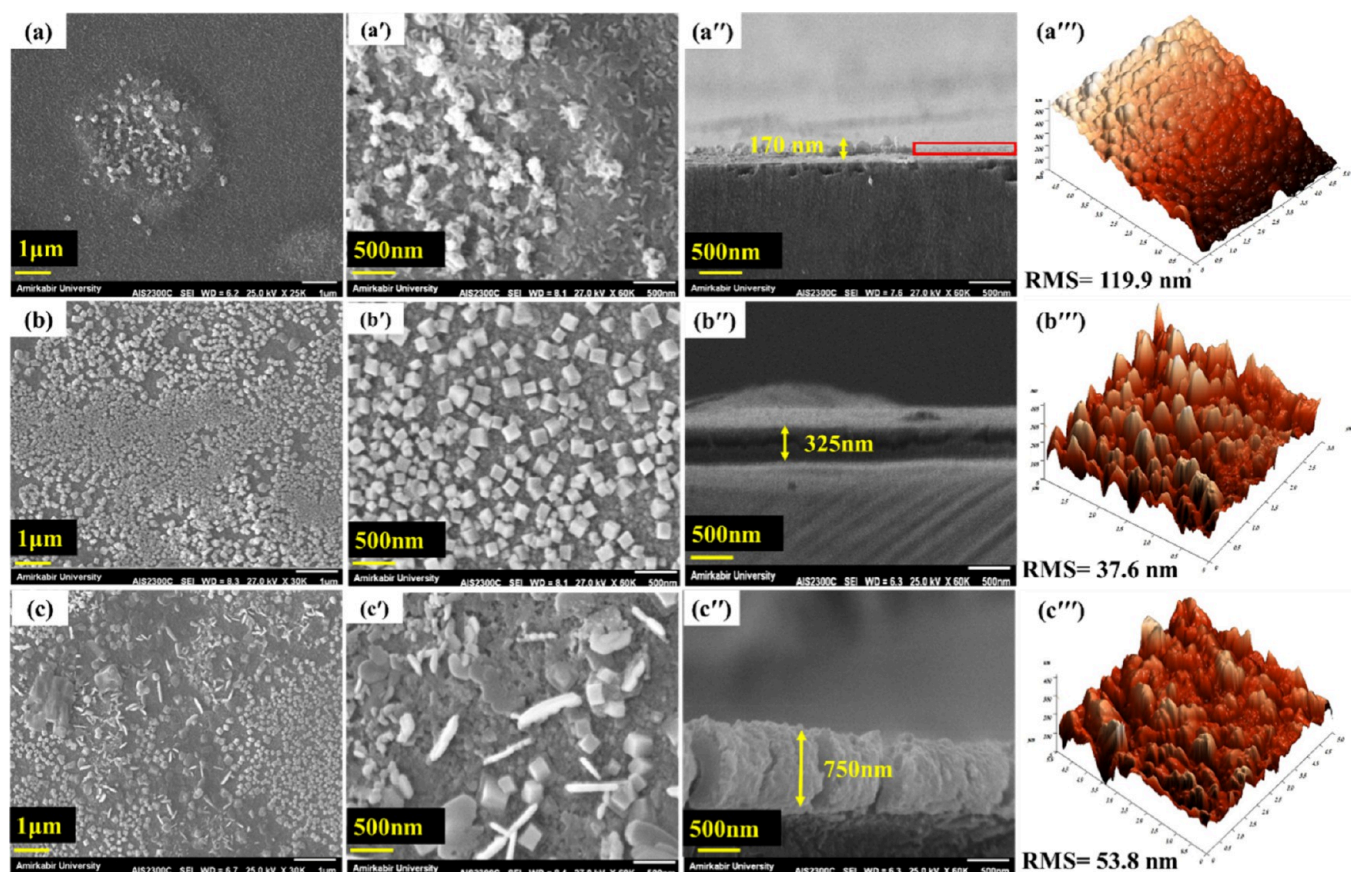


**Figure 3.** Longitudinal SEM images of (a, a') LNO-TF/ED-T1, (b, b') LNO-TF/ED-T2, and (c, c') LNO-TF/ED-T4 at two different magnifications, (a''–c'') associated cross-sectional SEM images, and (a'''–c''') AFM 3D height images.

The UV–vis absorption spectra of the LNO-P/SG-600 and LNO-P/ED-600 samples obtained in a dispersion media

consisting of  $\text{H}_2\text{O}:\text{C}_2\text{H}_5\text{OH}$  (1:1  $v/v$ ) with a concentration of 0.2 mM are illustrated in Figure 1b. The LNO-P/ED-600

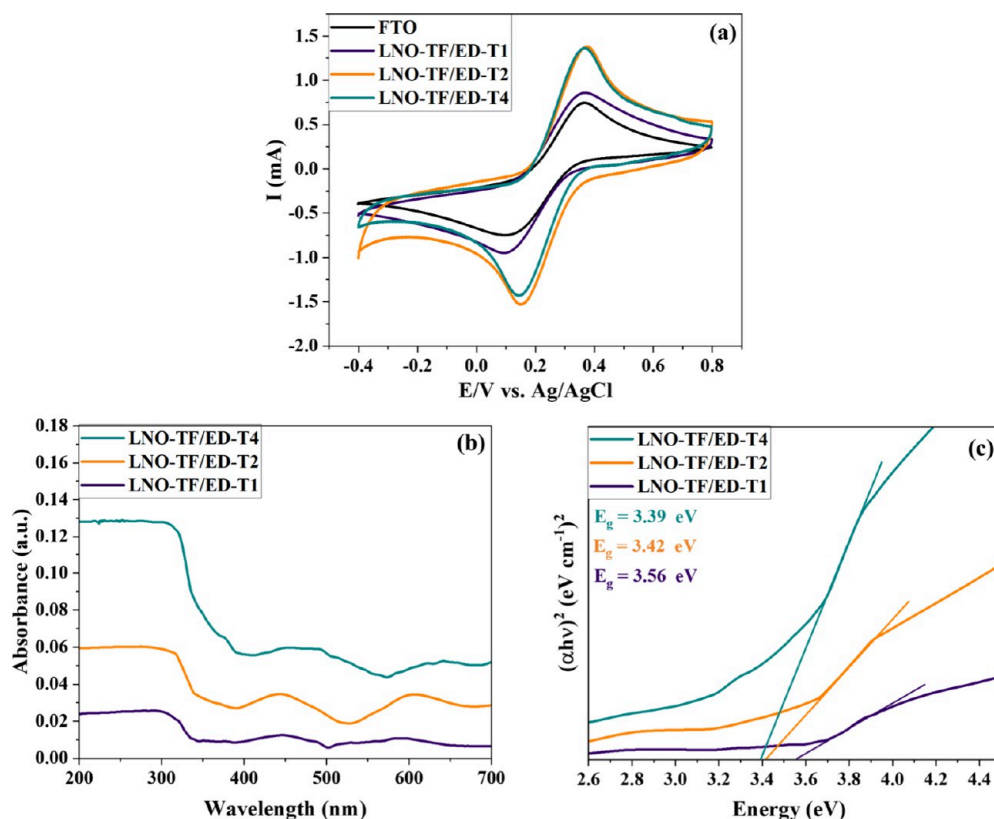


**Figure 4.** (a) CV response of bare FTO, LNO-TF/ED-T1, LNO-TF/ED-T2, and LNO-TF/ED-T4 samples in 0.1 M KCl containing 5.0 mM  $[\text{Fe}(\text{CN})_6]^{3-/4-}$ . (b) UV-vis absorption spectra of the indicated samples and (c) the corresponding Tauc's plots.

sample exhibits a lower absorption intensity than the LNO-P/SG-600 sample, while both samples display a significant absorption peak in the UV region. The higher absorption of the LNO-P/SG-600 sample is attributed to the larger sizes of the acquired nanoparticles in this sample (see Figure 2a",b"). The UV-vis spectra of the synthesized samples were utilized to estimate their optical band gap, employing Tauc's plot methodology. The estimation of the optical band gap values of the samples was carried out based on a  $(\alpha h\nu)^2$  versus  $h\nu$  (energy) plot (Figure 1c). This involved extrapolating a fitted straight line to the  $h\nu$  axis and determining the point at which it intersected to obtain the value of the band gap. The estimated optical band gaps of 3.37 and 3.67 eV for LNO-P/SG-600 and LNO-P/ED-600 samples are consistent with the literature value reported for LNO nanoparticles.<sup>20</sup> Based on the conducted research in the field of PSCs, compounds with optical band gaps ranging from 3 to 4 eV are currently being investigated as charge-transporting materials.<sup>20</sup> Therefore, the LNO nanostructures obtained from the earlier procedures described could be utilized to create a thin film, which can serve as a CTL in the PSC structure.

The morphology of the produced LNO samples was investigated by employing the SEM imaging technique. Figure 2a,a',b,b' shows the SEM images of the LNO-P/ED-600 and LNO-P/SG-600 powder samples, respectively. As can be seen, particles with a relatively more compact and bigger crystallite size were obtained for the LNO-P/SG-600 sample compared to the LNO-P/ED-600 sample, which confirmed the XRD results. Particle agglomeration could be ascribed to particles' high surface energy and small dimensions, which can lead to their easy merging to form clusters or aggregates.<sup>31</sup> In addition, the EDS spectra of the LNO-P/ED-600 and LNO-P/SG-600

are displayed in Figure S3a,b, respectively, which confirms the presence of La, Ni, and O elements within the synthesized samples.

Furthermore, TEM analysis was performed to further investigate the crystallite size of the synthesized nanoparticles. The TEM images of the LNO-P/SG-600 and LNO-P/ED-600 particle samples are presented in Figure 2a",b", respectively. These images demonstrate nanocrystals with mean particle sizes of 35 and 92 nm for LNO-P/ED-600 and LNO-P/SG-600 samples, respectively, validating the crystallite size estimation determined through XRD analysis.

### 3.2. Influence of the ED Duration on LNO Thin Films.

The physical and electrochemical features of the developed LNO thin films were tracked using SEM, AFM, UV-vis spectroscopy, and CV techniques to investigate the impacts of the time on the ED process. The surface morphology of the electrodeposited LNO-TF/ED-T1, LNO-TF/ED-T2, and LNO-TF/ED-T4 samples, prepared by applying  $-1.18$  V at 1, 2, and 4 min, are compared in Figure 3a-c,a'-c', respectively. As shown in Figure 3a,a', SEM images revealed that performing ED for 1 min in the LNO-TF/ED-T1 sample resulted in the inappropriate development of LNO nanostructures that covered a tiny proportion of the FTO electrode surface area. The SEM images in Figure 3b,b',c,c' reveal that the LNO-TF/ED-T2 sample resulted in uniformly shaped LNO nanocubes, while the LNO-TF/ED-T4 sample displayed an irregular morphology, which is likely attributed to the prolonged deposition time. Additionally, compared with LNO-TF/ED-T2, in the case of LNO-TF/ED-T4, increasing the deposition time to 4 min resulted in a compact thicker layer. As shown in Figure S4a, the LNO-TF/ED-T4 thin film exhibited a wide range of diameters in LNO nanostructures

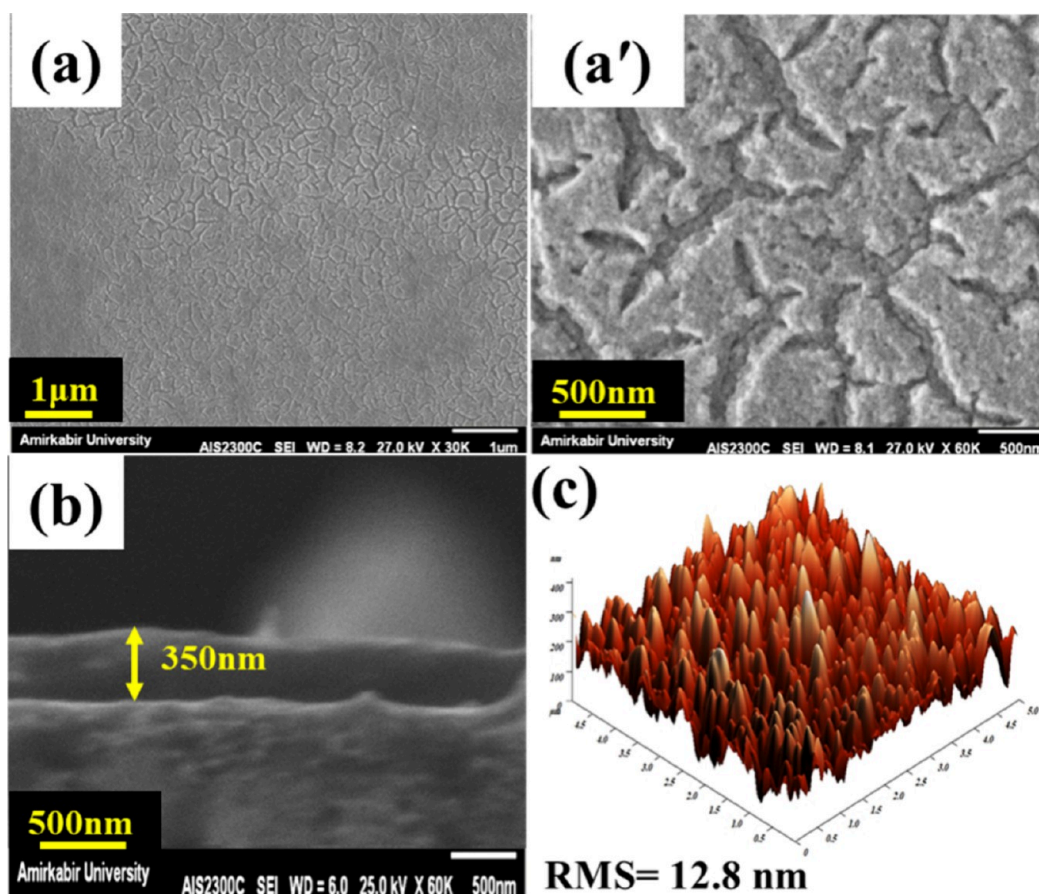


**Figure 5.** (a, a') Longitudinal SEM images at two magnifications, (b) corresponding cross-sectional SEM image, and (c) AFM 3D height images of the LNO-TF/ED-V1 sample.

with an average diameter of approximately  $183 \pm 133.23$  nm. It can be inferred that the prolonged ED duration in this sample has significantly influenced the enlargement of the produced nuclei, resulting in bigger nanoparticles with a broader size distribution, owing to additional nucleation and growth event occurrence.<sup>32</sup> On the other hand, the LNO nanoparticles in the LNO-TF/ED-T2 sample displayed a narrower diameter distribution with an average diameter of  $82 \pm 32.78$  nm (see Figure S4b). The cross-sectional SEM image of the LNO-TF/ED-T1 sample shown in Figure 3a'' revealed that some regions on the electrode surface were partially covered at around 170 nm, while other areas depicted in the image by a box with a red color outline appeared to be FTO without any deposited LNO nanostructures. Based on the illustrated image in Figure 3b'', the thickness of LNO in LNO-TF/ED-T2 was estimated to be approximately 325 nm. However, a higher thickness of 750 nm was observed for LNO-TF/ED-T4, which exceeds the acceptable thickness for CTLs in PSCs (see Figure 3c'').<sup>16,17</sup>

AFM was carried out to study the effect of the ED duration on the surface topography and surface roughness of LNO-TF/ED samples. It has been demonstrated that the surface roughness of the constituting layers significantly affects the photovoltaic characteristics of the PSCs and that CTLs possessing smoother surface morphology improve the PCE of PSCs.<sup>33</sup> Generally, this has been attributed to decreased interfacial trap density, improved interfacial contact between the CTL and the active layer, and reduced leakage current.<sup>34</sup> Figure 3a'''–c''' exhibits the three-dimensional (3D) height AFM images of the LNO-TF/ED-T1, LNO-TF/ED-T2, and

LNO-TF/ED-T4 samples, respectively. In terms of surface roughness, the LNO-TF/ED-T2 sample prepared in 2 min had a value of approximately 37.6 nm. This value was 30.11% lower than the surface roughness observed for the LNO-TF/ED-T4 sample (53.8 nm) and 68.6% lower than the LNO-TF/ED-T1 sample (119.9 nm). The results indicated that extending the ED duration led to an increase in both the thickness and surface roughness of the LNO thin film. Specifically, the LNO-TF/ED-T4 sample exhibited a higher surface roughness than the LNO-TF/ED-T2 sample. LNO-TF/ED-T1 exhibited the highest surface roughness due to the non-uniform aggregation or clustering of LNO nanoparticles on the partially covered FTO surface as well as differences in surface chemistry and properties. These differences lead to varying adhesion forces between the AFM tip and the surface, ultimately resulting in a higher surface roughness.<sup>35</sup>

Electrodeposited LNO samples were compared to bare FTO regarding their electrochemical surface area utilizing the Randles–Sevcik equation (eq S3) by monitoring the redox reaction of  $[\text{Fe}(\text{CN})_6]^{3-/4-}$  on the surface of LNO-TF/ED-T1, LNO-TF/ED-T2, and LNO-TF/ED-T4 samples independently. Figure 4a demonstrates that the LNO-coated electrodes typically delivered a greater current compared to the bare FTO electrode. The maximum current density was provided by LNO-TF/ED-T2 prepared in the deposition time of 2 min. The LNO-TF/ED-T4 sample showed a slight decrease in the current density compared to LNO-TF/ED-T2 due to its nonuniform and compact surface coverage, which was caused by an increase in the deposition time to 4 min. The lowest

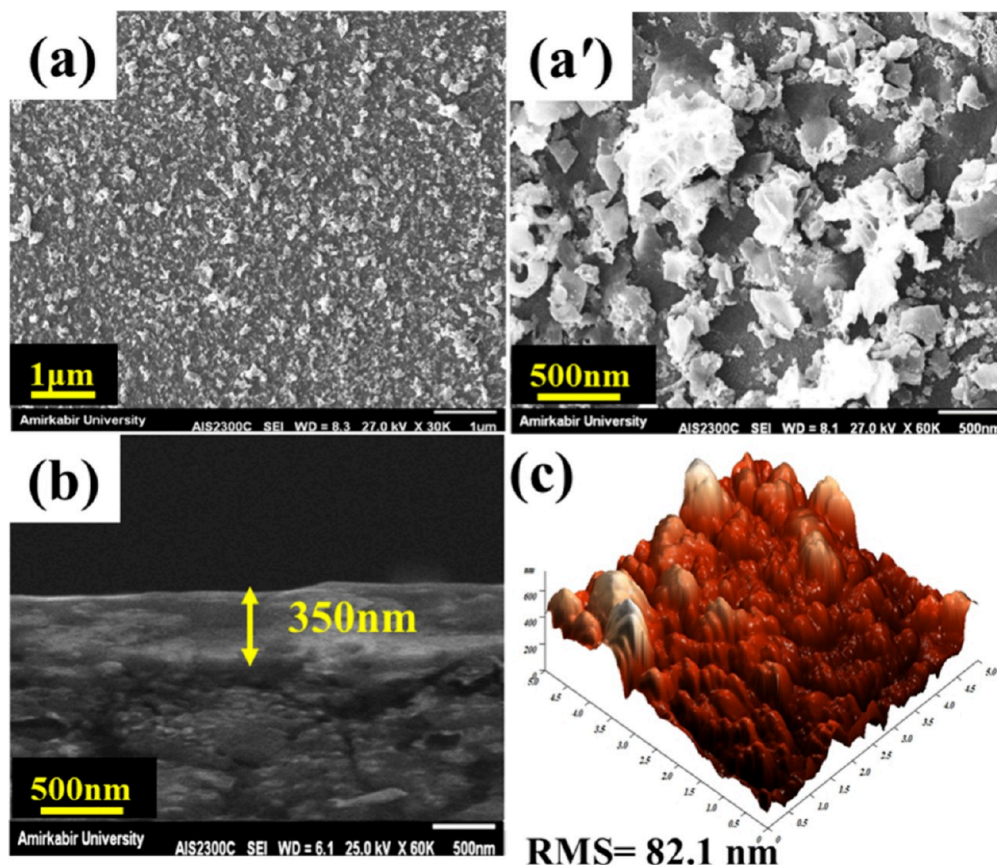


**Figure 6.** (a, a') Longitudinal SEM images at two magnifications, (b) corresponding cross-sectional SEM image, and (c) AFM 3D height images of the LNO-TF/SG sample.

current density was recorded for the LNO-TF/ED-T1 sample, which was higher than the bare FTO but less than the LNO-TF/ED-T2 and LNO-TF/ED-T4 samples, indicating that the electrode was not sufficiently covered by LNO nanostructures in 1 min. The highest current of the LNO-TF/ED-T2 sample was attributed to the higher accessibility of active sites, resulting in its more reversible pattern. The current intensity of the indicated thin films was used to estimate their electroactive surface area. The findings revealed that the LNO-TF/ED-T2 sample had the largest value of 1.241 cm<sup>2</sup>, exhibiting a 2.41 and 38.1% increase over the electroactive surface areas of the LNO-TF/ED-T4 (1.211 cm<sup>2</sup>) and LNO-TF/ED-T1 (0.768 cm<sup>2</sup>) samples, respectively.

Figure 4b demonstrates the UV–vis absorption spectra for the LNO-TF/ED-T1, LNO-TF/ED-T2, and LNO-TF/ED-T4 samples. The LNO-TF/ED-T4 sample exhibited the highest absorption intensity. On the other hand, reducing the ED time to 2 and 1 min resulted in a lower absorption intensity in the order of LNO-TF/ED-T2 > LNO-TF/ED-T1. These observations were consistent with the results obtained from longitudinal and cross-sectional SEM images. Specifically, the thicker and denser coverage of LNO nanostructures on the electrode surface of LNO-TF/ED-T4 resulted in greater absorption than LNO-TF/ED-T2, whereas the LNO-TF/ED-T1 sample, which was not completely covered by the LNO nanostructures, exhibited the lowest absorption intensity. The energy gap between the upper edge of the valence band (created by the O 2p band) and the lower edge of the conduction band (created by the Ni 3d band) is known as the optical band gap.<sup>36</sup> The optical band gap of the prepared thin

films was estimated via Tauc's plots, as depicted in Figure 3c. Based on the obtained results, the optical band gap value increased in the order of LNO-TF/ED-T1 > LNO-TF/ED-T2 > LNO-TF/ED-T4 samples as the absorption intensity decreased. The LNO-TF/ED-T1 sample displayed the highest optical band gap value of 3.56 eV, which was 4.1% greater than that of LNO-TF/ED-T2 (3.42 eV), and 5.0% greater than the optical band gap of LNO-TF/ED-T4 (3.39 eV). The reduced optical band gap observed in the LNO-TF/ED-T4 sample can be ascribed to the presence of larger nanoparticles and its higher thickness when compared to the LNO-TF/ED-T2 sample.<sup>37,38</sup>

The transparency of hole-transporting materials is a crucial factor in the development of efficient standard PSCs. Therefore, the optical transmittance of the prepared samples as potential candidates of HTLs was evaluated based on their UV–vis spectra. Since the surface of the LNO-TF/ED-T1 was inappropriately covered with the LNO nanostructures, it was not considered for further analyses. Based on the obtained UV–vis spectra shown in Figure 4b, the LNO-TF/ED-T2 sample could be a promising candidate for use as a charge-transporting material due to its lower absorption (<0.1 au) and high optical transmittance values, which is comparable to the transparency of FTO electrode (~85%). On the other hand, based on the surface morphology and thickness analyses of the prepared LNO thin films, the LNO-TF/ED-T4 sample was found to have an unsuitable thickness and compact and heterogeneous surface structure, resulting in a lower transparency (78%), current intensity, and electroactive surface area than the LNO-TF/ED-T2 sample. Therefore, the superior

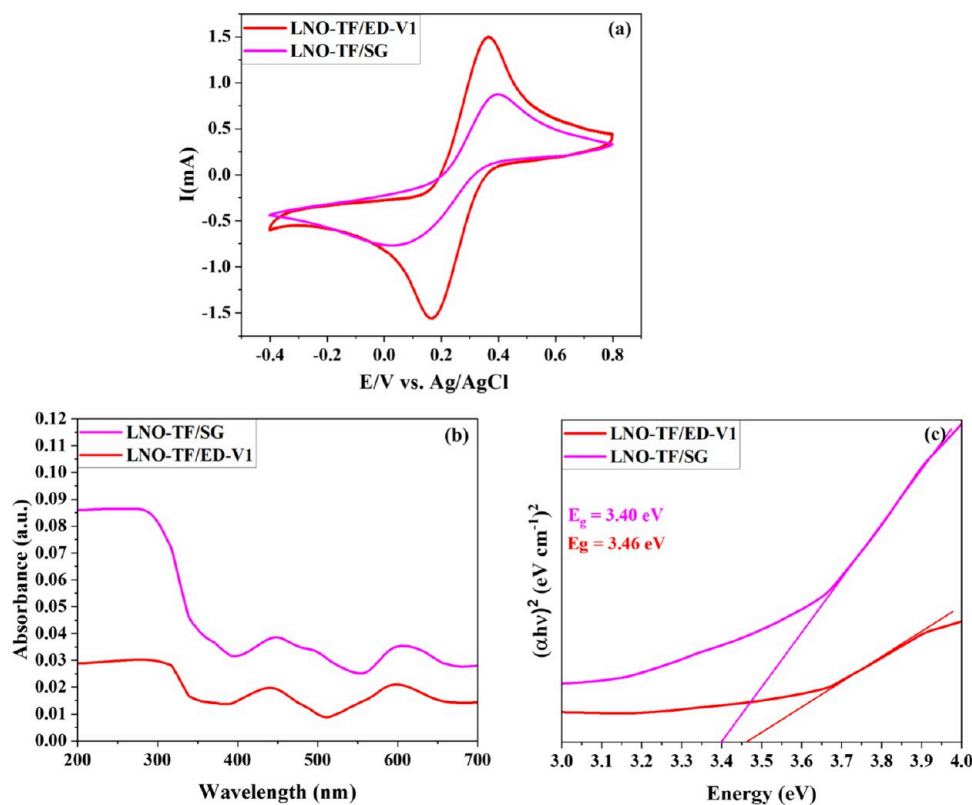


**Figure 7.** (a) CV response of LNO-TF/ED-V1 and LNO-TF/SG samples in 0.1 M KCl containing 5.0 mM  $[\text{Fe}(\text{CN})_6]^{3-/4-}$ . (b) UV-vis absorption spectra of the indicated samples and (c) corresponding Tauc's plots.

surface characteristics and improved current intensity of the LNO-TF/ED-T2 sample suggest that it has the potential to function as a better HTL in the structure of the PSC.

**3.3. Influence of the Electrolyte Stirring in ED on LNO Thin Films.** SEM images of LNO-TF/ED-V1 were displayed in Figure 5a,a' and compared to LNO-TF/ED-T2 presented in Figure 3b,b' to investigate the impact of electrolyte stirring on the morphology and thickness of the LNO thin film produced on the FTO electrode by ED. The size, surface morphology, and homogeneity of the electrodeposited LNO layer significantly changed by the mild stirring of the electrolyte solution during the ED process. As illustrated in Figure 5a, the LNO-TF/ED-V1 sample displayed a narrower size distribution of LNO nanoparticles with a smaller average diameter of  $32 \pm 5.11$  nm than the LNO-TF/ED-T2 sample ( $82 \pm 32.78$  nm) (refer to Figure S4b). Figure 5a,a' shows that a more uniform and smoother LNO thin film comprising smaller nanoparticles was formed under stirring in the LNO-TF/ED-V1 sample. Based on the proposed ED mechanism,  $\text{La}^{3+}$  and  $\text{Ni}^{2+}$  ions are precipitated as  $\text{La}(\text{OH})_3$  and  $\text{Ni}(\text{OH})_2$  on the surface of the electrode. The ions must be transferred to the electrode surface at a rate that does not exceed or is not lower than the deposition rate of  $\text{La}(\text{OH})_3$  and  $\text{Ni}(\text{OH})_2$  on the electrode surface; otherwise, the resulting LNO thin film will be nonuniform and weakly adhesive.<sup>32</sup> For the LNO-TF/ED-T2 sample (Figure 3b,b'), prepared under non-stirring conditions, the mass transport mechanism in the vicinity of the electrode surface is limited to the diffusion mechanism.<sup>32</sup> This results in a lower supply of  $\text{La}^{3+}$  and  $\text{Ni}^{2+}$  ions at the electrode surface, consequently decreasing the nucleation rate and nonuniform coverage of the FTO surface with bigger nanoparticles. In contrast, for the LNO-TF/ED-V1 sample,

prepared at a stirring rate of 100 rpm using the same potential of  $-1.18$  V, the convection mechanism seems to act as the main mass transport process and supports a higher ion concentration and nucleation rate at the electrode, leading to the formation of a more homogeneous LNO thin film with smaller particles in this sample (Figure 5a,a').

The comparison of the cross-sectional SEM images presented in Figures 3b'' and 5b reveals that the thickness of the LNO thin films experienced a slight increase when the electrolyte solution was subjected to mild stirring. In the LNO-TF/ED-V1 sample, the thickness of the deposited thin film reached 350 nm, which was approximately 7.14% higher than the thickness observed for the LNO-TF/ED-T2 sample prepared under unstirred conditions (325 nm). The AFM images presented in Figures 3b''' and 5c demonstrated a notable decrease in the surface roughness of the LNO thin film due to the electrolyte stirring. The surface roughness of LNO-TF/ED-T2 was reduced by 65.9% from 37.6 to 12.8 nm in LNO-TF/ED-V1. The mentioned morphological and topographical changes also resulted in a higher CV response of LNO-TF/ED-V1, as illustrated in Figure 7a. The given sample exhibited an increased electroactive surface area of  $1.341$   $\text{cm}^2$ , representing a 7.45% improvement compared to the electroactive surface area attained for LNO-TF/ED-T2 ( $1.241$   $\text{cm}^2$ ) (see Figure 4a). The more appropriate surface coverage of the FTO electrode by smaller LNO nanostructures ( $32 \pm 5.11$  nm) in the LNO-TF/ED-V1 sample led to a lower absorption intensity in the UV-vis spectrum and a rise in the optical band gap of this sample (see Figure 7b,c). According to Tauc's plots shown in Figure 7c, the optical band gap for the LNO-TF/ED-V1 was assessed to be approximately 3.46 eV, which was approximately 1.2% higher than that obtained for LNO-TF/

ED-T2 ( $E_g = 3.42$  eV) (Figure 4c). Furthermore, the determined optical transmittance of both samples was approximately identical to the FTO optical transmittance ( $\sim 85\%$ ) since the absorption of both samples was less than 0.1 au.

**3.4. Effects of the Potential Magnitude in ED on LNO Thin Films.** The deposition potential has substantial effects on the nucleation and growth rates. Consequently, this can indirectly lead to the formation of various morphologies and homogeneity of the LNO nanostructures on the FTO surface.<sup>39</sup> In order to evaluate the effect of potential magnitude, two other potentials of  $-1.13$  and  $-1.09$  V were also employed to carry out the ED process under stirring conditions in 2 min. These samples were named LNO-TF/ED-V2 and LNO-TF/ED-V3, and their properties were compared with those of the LNO-TF/ED-V1 sample. The impact of the deposition potential magnitude on the development of LNO film was investigated in terms of the physical and electrochemical features of the three indicated samples. Additional details and explanations can be found in Text S5.

**3.5. Comparing the LNO Thin Films Prepared by the Sol–Gel and ED Methods.** Morphological, optical, and electrochemical properties of LNO-TF/ED-V1 and LNO-TF/ED-T2 prepared by ED are compared with those of the sol–gel approach-based LNO thin layer (LNO-TF/SG) based on the different parts of Figures 3–7. As mentioned earlier, LNO-TF/SG was produced by spin-coating of the viscose solution of LNO acquired from the sol–gel process on the FTO electrode to a thickness of 350 nm since the thickness of the ED samples appeared to be in the range of 310–350 nm (see Figure 6b). Figure 6a,a' exhibits the surface morphology of the LNO thin film produced by the sol–gel process. As shown, the deposited film showed the presence of scattered, nonuniform, and incomplete coverage of the LNO nanoparticles on the surface of the FTO electrode. Furthermore, according to Figure S5d, the LNO-TF/SG thin film had the highest diameter distribution and average diameter of LNO nanoparticles, which was estimated to be  $153 \pm 105.02$  nm. In comparison, the average diameters of LNO nanoparticles in the LNO-TF/ED-T2 and LNO-TF/ED-V1 samples were  $82 \pm 32.78$  nm and  $32 \pm 5.11$  nm, respectively (see Figures S4b and S5a). Based on the AFM image of LNO-TF/SG shown in Figure 6c, the surface roughness of this sample (82.1 nm) was approximately 84.4% higher than that observed for LNO-TF/ED-V1 (12.8 nm) and 54.2% higher than the roughness of the LNO-TF/ED-T2 sample (37.6 nm). The findings suggest that the spin-coating method was unable to produce a uniformly coated LNO-TF/SG sample. In contrast, the ED method was observed to be more effective than the spin-coating method, yielding LNO thin films that were better suited for use as the CTL in PSCs. The morphology and surface roughness of the active layer (P3HT:PCBM)-coated LNO thin films were also investigated, and the obtained AFM images are illustrated in Figure S8. The findings reveal that the surface roughness values for LNO-TF/ED-V1, LNO-TF/ED-T2, and LNO-TF/SG samples are 6.2, 18.2, and 32.7 nm, respectively. This indicates a significant reduction in the surface roughness for various FTO/LNO layers after the active layer was spin-coated on it. However, the surface roughness is higher than that obtained for FTO/PEDOT:PSS systems reported as an HTL in the literature. The slightly rougher surface morphology can enhance the interfacial properties and increase the contact area with the active layer, promoting improved charge

transport and collection efficiency.<sup>40</sup> Moreover, the nucleation and self-organization of the photoactive layer can be influenced by the higher roughness of the LNO.<sup>41,42</sup> The increased self-organization is anticipated to enhance the phase separation of P3HT within the blend with P3HT chains forming an ordered structure to boost hole mobility significantly. Simultaneously, the aggregation of fullerene molecules establishes distinct pathways for efficient electron transport. This nanoscale phase separation is expected to contribute to the enhancement of the short-circuit current ( $J_{sc}$ ) in PSCs.<sup>42</sup> This modification is also advantageous in establishing solid contact with the top active layer and preventing its diffusion into HTL for maintaining device efficiency and stability.<sup>43</sup>

As Figure 7b shows, the LNO-TF/ED-V1 demonstrated the lowest absorption intensity, which was related to the above-explained reasons mentioned in Section 3.4. The highest absorption was found for the LNO-TF/SG sample, while the absorption of LNO-TF/ED-T2 was between LNO-TF/ED-V1 and LNO-TF/SG samples. Furthermore, as the absorption of all samples was less than 0.1 au, the estimated optical transmittance for LNO-TF/ED-T2, LNO-TF/ED-V1, and LNO-TF/SG samples was considered to be around that of the FTO electrode ( $\sim 85\%$ ). As demonstrated in Figures 4c and 7c, the optical band gap of the LNO-TF/ED-T2, LNO-TF/ED-V1, and LNO-TF/SG samples was estimated based on Tauc's plots, and the results are listed in Table S5.

The chemical composition, crystal structure, and grain diameter of a material can significantly influence its band gap.<sup>37</sup> The mentioned influencing factors, except for the grain size, remained constant for all the studied samples. Generally, the band gap value can be increased as a result of a grain size decrease. Quantum confinement causes a change in the band gap with increasing the grain size, which may be explained by the following equation<sup>37</sup>

$$E_g^{\text{nano}} = E_g^{\text{bulk}} + \frac{h^2 \Gamma^2}{2Mr^2} \quad (1)$$

where  $E_g^{\text{nano}}$  denotes the nanoparticles' band gap and  $E_g^{\text{bulk}}$  shows the bulk-material band gap.

$M$  represents the effective mass of the system, and  $r$  indicates the nanoparticle radius. As previously explained and confirmed by the SEM images, the smallest grain size of  $32 \pm 5.11$  nm was obtained for the LNO-TF/ED-V1 sample. Therefore, the highest optical band gap was obtained for the LNO-TF/ED-V1 (3.46 eV) sample, while the smallest band gap (3.40 eV) was obtained for the LNO-TF/SG sample with the largest particle size of  $153 \pm 105.02$  nm. The LNO-TF/ED-T2 sample prepared without stirring and with an average nanoparticle diameter of  $82 \pm 32.78$  nm exhibited an optical band gap of 3.42 eV.

According to Figure 7a, LNO-TF/SG exhibited a significantly lower current intensity and electroactive surface area ( $0.781$  cm<sup>2</sup>) compared to the LNO-TF/ED-V1 and LNO-TF/ED-T2 (Figure 4a) samples prepared by ED due to the improper and nonuniform deposition of LNO nanostructures using the spin-coating method. As a result of its more uniform surface coverage, LNO-TF/ED-V1 displayed the highest current density and electroactive surface area ( $1.341$  cm<sup>2</sup>), which was approximately 7.45% higher than that of LNO-TF/ED-T2 prepared in unstirred conditions and 41.75% higher than the current density obtained for the LNO-TF/SG sample ( $0.781$  cm<sup>2</sup>).

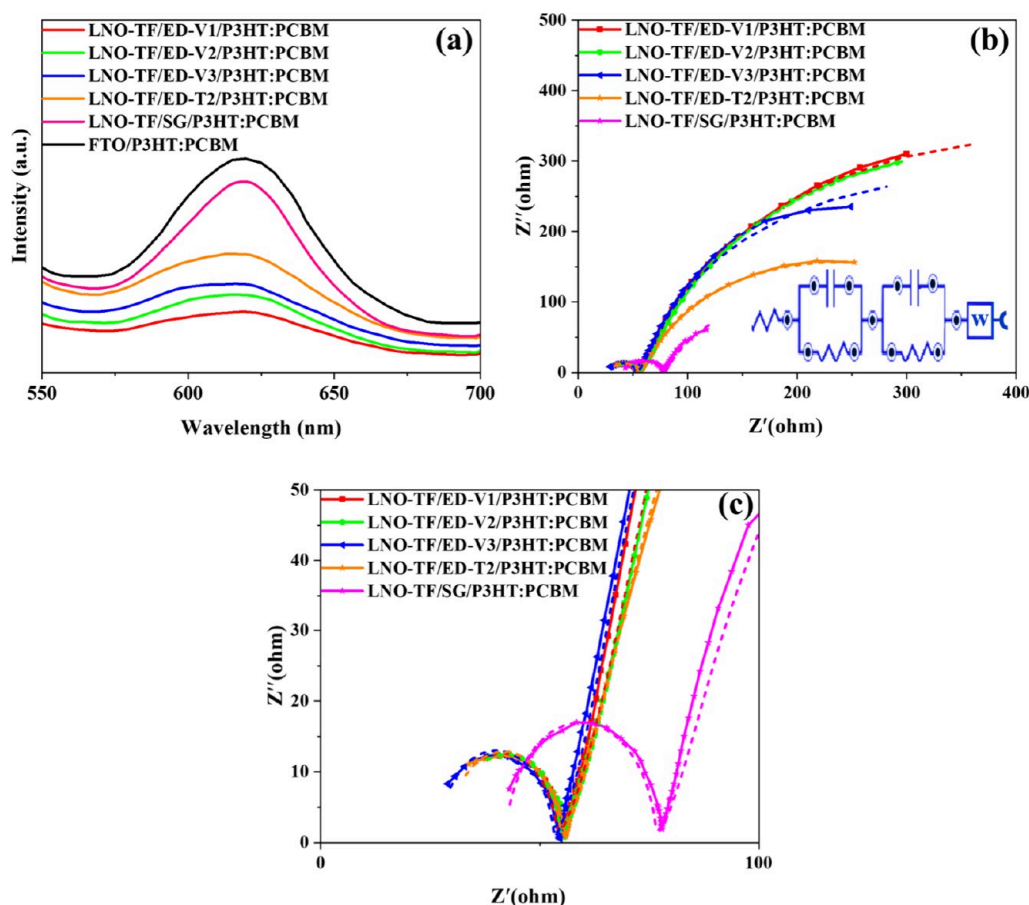


**Figure 8.** (a) PL spectra and (b) Nyquist plots obtained in  $\text{LiClO}_4$  solution (0.1 M acetonitrile) including 5.0 mM  $[\text{Fe}(\text{CN})_6]^{3-/4-}$  as the electrolyte of the FTO/P3HT:PCBM and FTO/LNO/P3HT:PCBM samples along with corresponding fitted lines represented in dashed lines. (The inset depicted in b illustrates the equivalent circuit used for fitting the EIS data.) (c) Section of Nyquist plots in the frequency ranging from 0 to 100 kHz.

**3.6. Influence of LNO Thin-Film Synthesis Parameters on Charge Carrier Recombination.** The charge carrier density, mobility, and recombination rate significantly impact the photovoltaic performance of PSCs.<sup>44</sup> Utilizing PL spectroscopy, the photoluminescence characteristics of the prepared samples covered with a thin layer of P3HT:PCBM (active layer) were evaluated to track the effects of investigated synthesis variables on the charge carriers' recombination rate in the active layer. Figure 8a represents the PL spectra of the prepared sol-gel and ED-based LNO samples and the FTO/P3HT:PCBM sample containing no LNO thin layer. The increased rate of charge carrier recombination increases the intensity of the PL emission. As can be seen, the FTO/P3HT:PCBM sample demonstrated the maximum PL intensity due to the higher charge recombination. The PL spectra exhibited a prominent emission peak at 620 nm, which is a distinctive emission peak associated with the conjugated  $\pi$ -system. The observed peak could be ascribed to the phenomenon of excited  $\pi$ -electrons undergoing relaxation to their respective ground state.<sup>16,17</sup> The samples consisting of LNO (FTO/LNO/P3HT:PCBM) showed the same peak but with significantly lower intensities. The observed improvement in charge carrier recombination was ascribed to the positive effect of the LNO layer, which facilitated the transfer of charges between the P3HT:PCBM and LNO layers, leading to a decrease in recombination.<sup>45</sup> The excitation wavelength used in the photoluminescence (PL) measurements, which includes

430 nm (2.90 eV), was insufficient in terms of photon energy to generate excitons inside the LNO layer. Consequently, the thin film composed of P3HT:PCBM is merely subjected to optical excitation. This outcome can be ascribed to the fact that the optical band gap of the synthesized LNO layer is higher than the provided photon energy.<sup>16</sup> The LNO-TF/ED-V1/P3HT:PCBM sample displayed the lowest PL emission, as shown in Figure 8a, indicating an improvement in charge transfer between the LNO and P3HT:PCBM layers and a reduction in recombination of charge carriers. This is probably the outcome of the smoother surface morphology, enhanced interface contact area, better energy level alignment with the active layer, and more ordered structure of this sample. Other samples demonstrated higher PL emissions in the order of FTO/P3HT:PCBM > LNO-TF/SG/P3HT:PCBM > LNO-TF/ED-T2/P3HT:PCBM > LNO-TF/ED-V3/P3HT:PCBM > LNO-TF/ED-V2/P3HT:PCBM > LNO-TF/ED-V1/P3HT:PCBM. These findings indicated that employing LNO as the HTL can considerably decrease the rate of charge recombination. Based on these observations, the LNO-TF/ED-V1/P3HT:PCBM sample seemed to be a preferable candidate for the HTL because it can effectively suppress charge recombination and consequently facilitates a more effective charge transfer through the PSC.

EIS measurements were carried out to evaluate the effects of the investigated variables during the preparation of LNO as the HTL on the charge mobility and charge transfer resistance at

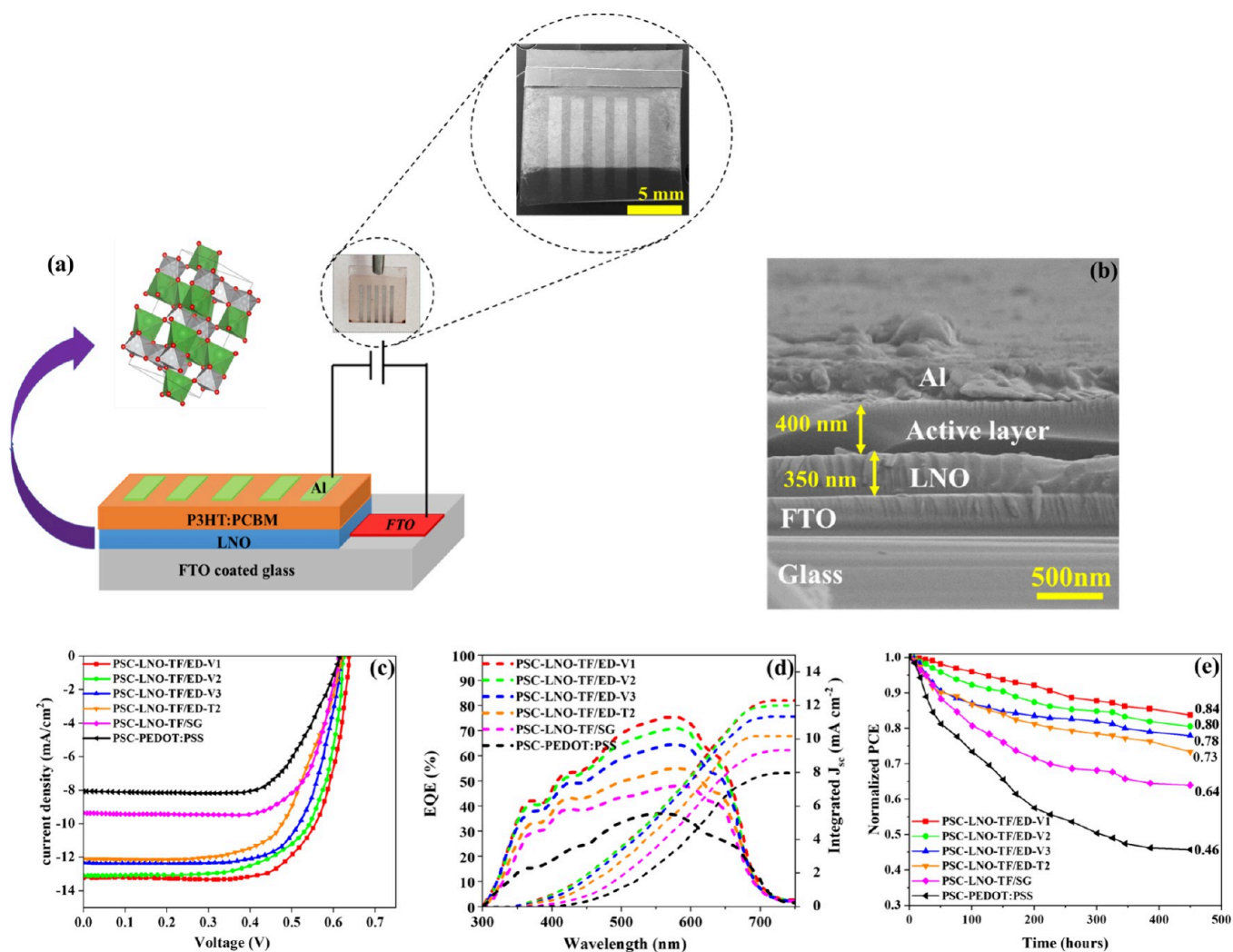


**Figure 9.** (a) Schematic illustration along with a digital photo and a top view FESEM image of a manufactured PSC utilizing LNO as the HTL; (b) backscatter FESEM cross-sectional image of the PSC-LNO-TF/ED-V1 device; (c)  $J$ - $V$  curves under  $100 \text{ mW cm}^{-2}$  AM 1.5 illuminations. (d) EQE plots of the constructed PSCs and (e) air stability without encapsulation in an ambient environment.

the FTO/LNO/P3HT:PCBM interfaces. Figure 8b displays a comparison of the Nyquist plots of the produced samples. The equivalent circuit model of  $[R(\text{CR})(\text{CR})W]$  is depicted as an inset in Figure 8b, which provided the best match to the extracted impedance data (chi-square of  $10^{-4}$ ). As shown, the Nyquist plots of the samples displayed two semicircles, indicating the presence of two interfacial processes. The high-frequency semicircle observed in the Nyquist plots was associated with the charge transfer occurring between the active layer and the LNO nanostructures, whereas the low-frequency semicircle was related to the interface of P3HT and PCBM compounds in the active layer.<sup>46,47</sup> The corresponding information acquired from the Nyquist plots is displayed in Table S4. The resistance values between P3HT and PCBM ( $R_2$ ), LNO and P3HT:PCBM ( $R_1$ ), and the contacts within the solution ( $R_s$ ) are all represented. Therefore, the decrease in  $R_1$  values and increase in  $R_2$  values indicate a better charge transfer mechanism at the junctions of LNO nanostructures and the active layer as well as a decreased rate of charge recombination at the P3HT and PCBM interfaces. The LNO-TF/SG/P3HT/PCBM sample demonstrated the highest value for  $R_s$ , representing electrolyte and metal contact resistance, while the LNO-TF/ED-V3 sample displayed the lowest value

(see Table S4). The LNO-TF/ED-V1/P3HT:PCBM exhibited minimal charge transfer resistance due to the smallest  $R_1$  value obtained (see Figure 8c). Furthermore, the maximum charge recombination resistance ( $R_2$ ) was recorded for the LNO-TF/ED-V1/P3HT:PCBM sample. The presented data in Table S4 shows that the LNO-TF/SG/P3HT/PCBM demonstrated the minimum value for the  $R_2$  and the maximum value for the charge transfer resistance ( $R_1$ ). The Warburg parameter ( $W$ ) characterizes the one-dimensional diffusion of ions in the semi-infinite state. Assuming an infinite thickness of the diffusion layer, this suggests that ion penetration is limited to just one dimension and is constrained by the substantial flat electrode on one side.<sup>48</sup> The low  $W$  values indicate that the diffusion at the interfaces is anomalous. This is more likely to happen whenever the surface roughness of the sample is higher, and ions are trapped in the holes for an extended time.<sup>49</sup> The AFM images in Figure 5a and Figure S8a indicated that the LNO-TF/ED-V1 sample possessed the lowest surface roughness. The EIS data in Table S4 revealed that this sample showed the greatest  $W$  of  $211.40 \text{ ohm s}^{-1/2}$ . The  $W$  value of LNO-TF/ED-V2, LNO-TF/ED-V3, LNO-TF/ED-T2, and LNO-TF/SG samples decreased by 24.5, 39.3, 39.2, and 71.4%, respectively. These results support the observation from AFM images of the

corresponding samples that their surface roughness increased in the order of LNO-TF/ED-V2 < LNO-TF/ED-V3 < LNO-TF/ED-T2 < LNO-TF/SG. Considering the results, it can be inferred that the LNO-TF/ED-V1 sample demonstrated enhanced diffusion mechanisms at the interfaces between P3HT:PCBM and the electrolyte, which can be attributed to the comparatively smoother surface of LNO nanoparticles, better energy level alignment, and interface contact area in this sample.<sup>50</sup>

The estimation of charge mobility ( $\mu$ ) at the interfaces of LNO/P3HT:PCBM was carried out using eq S7. The mathematical calculation of charge mobility was conducted using  $R_1$  and  $C_1$  values obtained from the high-frequency semicircle.<sup>16</sup> The maximum charge mobility value of  $2.30 \times 10^{-6} \text{ cm}^2 \text{ V}^{-1} \text{ S}^{-1}$  was demonstrated by the LNO-TF/ED-V1/P3HT:PCBM sample, surpassing the values obtained for the other samples. Among the investigated samples, the LNO-TF/SG sample displayed the lowest charge mobility value of  $1.50 \times 10^{-7} \text{ cm}^2 \text{ V}^{-1} \text{ S}^{-1}$ . The acquired findings demonstrated that LNO nanoparticles improve charge mobility, increase charge recombination resistance, and decrease charge transfer resistance at surfaces. Generally, the charge mobilities of organic semiconductors are relatively lower than those of their inorganic counterparts.<sup>51</sup> Therefore, it is expected that LNO nanoparticles, particularly those used in the LNO-TF/ED-V1, could serve as a superior HTL in manufacturing normal BHJ PSCs compared to PEDOT:PSS.

**3.7. Characterization of the Fabricated LNO-Based PSCs.** The effect of the investigated parameters in the synthesis of LNO samples on the photovoltaic efficiency of PSCs was investigated by utilizing five different samples, namely, LNO-TF/ED-V1, LNO-TF/ED-V2, LNO-TF/ED-V3, LNO-TF/ED-T2, and LNO-TF/SG, as the HTL in a conventional structure of BHJ PSC constructed based on a P3HT:PCBM active layer. A schematic representation of the constituent parts of the BHJ PSCs utilizing LNO as the HTL along with a top-view FESEM image of the fabricated device is displayed in Figure 9a. The cross-sectional backscatter FESEM image of the device (Figure 9b) demonstrates the appropriate orientation of the layers in the following sequence of FTO/LNO/active layer/Al from bottom to top. The average thicknesses of LNO and photoactive layers are  $\sim 350$  and  $\sim 400$  nm, respectively. The current–voltage ( $J$ – $V$ ) curves of the manufactured PSCs are demonstrated in Figure 9c. As anticipated, the photovoltaic efficiency of the PSCs constructed using LNO-TF/ED-V1 as the HTL (PSC-LNO-TF/ED-V1) was significantly better than that of other constructed devices. The relevant photovoltaic parameters for investigated PSCs are presented in Table 1. The highest short-circuit current ( $J_{sc}$ ) of  $13.24 \text{ mA cm}^{-2}$ , open-circuit voltage ( $V_{oc}$ ) of  $0.64 \text{ V}$ , and a fill factor (FF) of 70% were obtained for PSC-

LNO-TF/ED-V1. This led to a PCE of 5.90, which was approximately 4.4%, 10.3%, 20.1%, 45.3%, and 73.5% higher than those values achieved for the fabricated PSC-LNO-TF/ED-V2, PSC-LNO-TF/ED-V3, PSC-LNO-TF/ED-T2, PSC-LNO-TF/SG, and PSC–PEDOT:PSS devices, respectively.

$J_{sc}$  in a solar cell is mainly affected by the number of charge carriers generated inside the active layer. The efficient utilization of incident light by the applied active layer can lead to high exciton generation. Thus, the high amount of light absorption, better energy level alignment, and an improved interface contact area of the active layer in PSC-LNO-TF/ED-V1 can result in a much better photovoltaic performance in this device. On the other hand, the open-circuit voltage,  $V_{oc}$ , is notably impacted by the process of charge recombination occurring at the interfaces.<sup>52</sup> The LNO-TF/ED-V1 sample exhibits a smoother and more uniform surface morphology, which is particularly evident after the application of the active layer (Figure S8). This characteristic is anticipated to improve the interface contact area with the active layer and facilitate enhanced charge transfer, leading to reduced charge recombination and higher values of  $J_{sc}$  and  $V_{oc}$ . Additionally, the higher conductivity of this sample also contributed to the enhanced efficiency of the PSC-LNO-TF/ED-V1.

External quantum efficiency (EQE) analyses were carried out on PSCs with LNO thin films developed under diverse circumstances as the HTL to investigate the impact of different synthesis parameters on the photovoltaic performance of P3HT:PCBM-based devices. EQE plots illustrate the devices' photon-current response as a wavelength function. It is typically determined by the number of photogenerated charge carriers that have been collected to the number of incident photons illuminated from a light source.<sup>53</sup> The EQE spectra of the BHJ PSCs constructed by employing PEDOT:PSS and prepared LNO samples as HTL and the integrated current diagrams are depicted in Figure 9d. The integrated  $J_{sc}$  values with the EQE curves correspond well and follow a similar trend to those in the  $J$ – $V$  measurements of PSCs. Moreover, a considerable consistency between cell characteristics and EQE measurements was observed for all fabricated solar cells. The photovoltaic performance of PSCs using LNO samples exhibited significantly greater EQE compared to the device using PEDOT:PSS as the HTL. Over the entire wavelength range, the EQE of the devices increased significantly in the order of PSC-LNO-TF/ED-V1 > PSC-LNO-TF/ED-V2 > PSC-LNO-TF/ED-V3 > PSC-LNO-TF/ED-T2 > PSC-LNO-TF/SG. The results were consistent with the trend observed in the decreasing performance of the constructed PSCs. The EQE of the PSC-LNO-TF/ED-V1 device was assessed to be around 75.3%, which was significantly more than that estimated for PSC-LNO-TF/ED-V2 (70.1%), PSC-LNO-TF/ED-V3 (64.4%), PSC-LNO-TF/ED-T2 (55.1%), and PSC-LNO-TF/SG (48.1%). The PSC–PEDOT:PSS device demonstrated the minimum value of EQE (37.1%). The improvements in EQE were attributed to the enhancements in mobility, charge accumulation, and light absorption achieved through the modifications made in the study.<sup>53</sup> Hence, the enhanced light absorption, charge carrier separation, transport, and collection in the LNO-TF/ED-V1 layer as well as its enhanced interface contact area, superior surface uniformity, and energy level properties contributed to the increased  $J_{sc}$  observed in the PSC with this constituent layer. The study results suggest that LNO-TF/ED-V1 could meet the requirements of a promising candidate for use as the HTL in PSCs.

**Table 1. Photovoltaic Parameters Extracted from the  $J$ – $V$  Curves of the Prepared PSCs**

name	$J_{sc}$ ( $\text{mA cm}^{-2}$ )	$V_{oc}$ (V)	FF (%)	PCE (%)
PSC-LNO-TF/ED-V1	13.24	0.64	70	5.90
PSC-LNO-TF/ED-V2	13.10	0.63	69	5.65
PSC-LNO-TF/ED-V3	12.32	0.62	70	5.35
PSC-LNO-TF/ED-T2	12.10	0.62	65	4.88
PSC-LNO-TF/SG	9.36	0.61	71	4.06
PSC–PEDOT:PSS	8.10	0.62	68	3.40

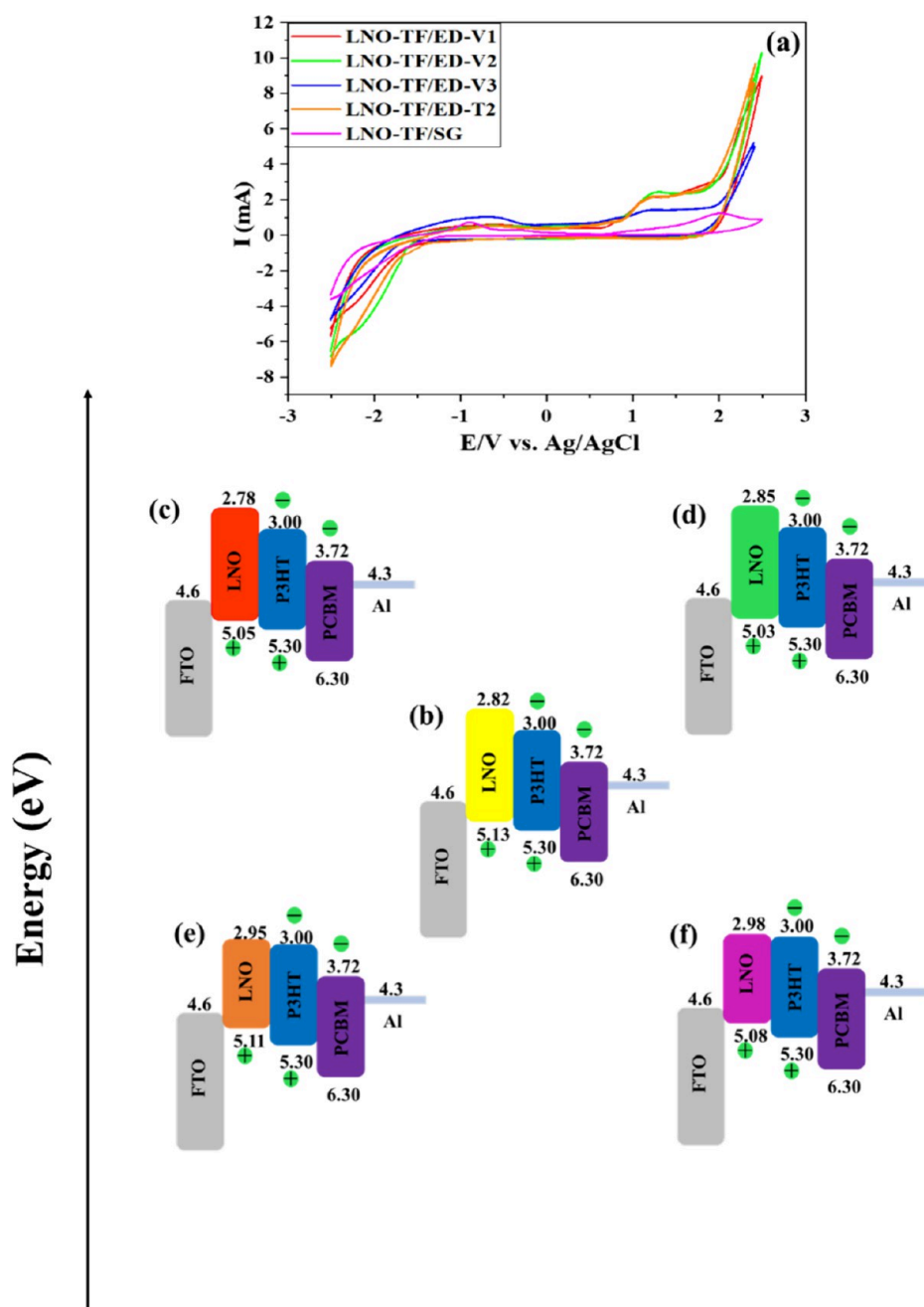


**Figure 10.** (a) CV responses in acetonitrile-based 0.1 M KClO<sub>4</sub> solution for LNO-TF/ED-V1, LNO-TF/ED-V2, LNO-TF/ED-V3, LNO-TF/ED-T2, and LNO-TF/SG samples. Energy level diagram of PSCs (b) FTO/LNO-TF/ED-V1/P3HT:PCBM/Al, (c) FTO/LNO-TF/ED-V2/P3HT:PCBM/Al, (d) FTO/LNO-TF/ED-V3/P3HT:PCBM/Al, (e) FTO/LNO-TF/ED-T2/P3HT:PCBM/Al, and (f) FTO/LNO-TF/SG/P3HT:PCBM/Al.

While PSCs have not yet achieved their expected maximum efficiency, long-term stability has become a prominent issue in extending their technology from academic research to commercial applications.<sup>54</sup> To further understand the influence of manufactured LNO thin films as HTLs on device stability compared to reference PEDOT:PSS, the long-term stability of unencapsulated P3HT:PCBM-based devices under ambient conditions was explored. It should be mentioned that the stability of PSCs can be significantly influenced by changes in the charge-transporting layers. Figure 9e demonstrates the assessment outcomes of environmental stability for the corresponding PSC devices based on LNO HTLs in an ambient condition (at 20 °C and 20–30% relative humidity).

The aging measurements were performed at regular intervals for 450 h. The value of PCEs were normalized to their  $t = 0$  values. The results revealed that incorporating LNO into the structure of the cells improves the stability of the device. As can be seen in Figure 9e, after 450 h of aging at ambient conditions, the devices fabricated based on the electro-deposited LNO thin films consisting of PSC-LNO-TF/ED-V1, PSC-LNO-TF/ED-V2, PSC-LNO-TF/ED-V3, and PSC-LNO-TF/ED-T2 retained 84, 80, 78, and 73% of their initial performance, respectively. As expected, the performance of the unencapsulated PSC-LNO-TF/SG device decreased more rapidly, and the PCE of the device decreased to 64% of the original value. The findings clearly demonstrate that the

**Table 2. Performance Comparison of Devices Based on Different HTL Materials with the Best PSC Prepared in This Work**

structure of the device	HTL-prepared method/layer morphology	$J_{sc}$ (mA cm <sup>-2</sup> )	$V_{oc}$ (V)	FF (%)	PCE (%)	ref
ITO/NiO/P3HT:PCBM/Ca/Al	spin-coating/thin film	8.60	0.58	71.00	3.60	57
ITO/NiO/P3HT:PCBM/BCP/LiF/Al	thermal evaporation/thin film	12.31	0.65	44.50	3.54	58
ITO/NiO/P3HT:PCBM/Al	electrodeposition/thin film	10.95	0.64	60.14	4.21	17
ITO/CuO <sub>x</sub> /P3HT:PCBM/Ca/Al	spin coating/thin film	10.10	0.63	64.70	4.14	59
FTO/Cu <sub>2</sub> O/P3HT:PCBM/Ca/Al	thermal evaporation/thin film	9.52	0.57	53.11	2.88	60
ITO/MoO <sub>3</sub> /P3HT:PCBM/Al	spin coating/thin film	10.70	0.59	63.70	4.02	61
ITO/MoO <sub>3</sub> /P3HT:PCBM/Al	spray deposition/nanostructure	10.00	0.57	47.40	2.80	62
FTO/V <sub>2</sub> O <sub>5</sub> /P3HT:PCBM/Al/Ag	spin coating/thin film	9.60	0.53	58.9	3.00	63
ITO/V <sub>2</sub> O <sub>5</sub> /P3HT:PCBM/Al	electrodeposition/thin film	9.43	0.56	65.00	3.40	16
ITO/CuGaO <sub>2</sub> /P3HT:PCBM/Ca/Al	spin coating/thin film	9.18	0.54	65.00	3.20	64
ITO/CuCrO <sub>2</sub> /PCDTBT:PCBM/Ca/Al	drop coating/nanocrystal	9.31	0.87	60.00	4.86	65
FTO/LaNiO <sub>3</sub> /PTB7Th:PC71BM/LiF/Al	spin coating/thin film	18.26	0.78	56.60	9.45	20
FTO/LaNiO <sub>3</sub> /P3HT:PCBM/Al	electrodeposition/thin film	13.24	0.64	70.00	5.90	this work

stability of P3HT:PCBM-based devices was greatly enhanced by incorporating LNO thin films prepared by the ED approach. At the same time, the PCE of the reference cell (PSC–PEDOT:PSS) decreased remarkably after 450 h and reached about 46% of its initial PCE. The low efficiency in PSCs is frequently associated with the degradation of organic compounds resulting from exposure to oxygen or water.<sup>54</sup> Furthermore, as previously mentioned, the acidic and hydrophilic characteristics of PEDOT:PSS reduces the stability of these devices. As a nonacidic inorganic ternary perovskite oxide, LNO is commonly considered to be a more appropriate compound than organic PEDOT:PSS to enhance the stability of PSCs. Our findings also demonstrated that PSCs based on LNO perovskite oxide were more promising for practical applications than PEDOT:PSS-based devices. The results obtained from the light stability assessment of the manufactured solar cells correspond with the anticipated outcomes and are in alignment with other tests conducted on the fabricated solar cells. According to the CV measurements of the samples in an acetonitrile-based solution (Figure 10a), eqs S4–S6 were used to determine the energy levels and electrochemical band gap of the LNO thin films. The test results, including the calculated values of  $E_v$ ,  $E_c$ ,  $E_g$ , and the determined  $E_{ox}$  and  $E_{red}$  values for the LNO samples, are illustrated in Table S5. As can be seen, the calculated electrochemical band gap  $E_g$  increased from LNO-TF/SG (2.10 eV) to LNO-TF/ED-V1 (2.31 eV). The estimated values of  $E_g$  for LNO-TF/ED-V2, LNO-TF/ED-V3, and LNO-TF/ED-T2 samples are 2.26, 2.18, and 2.16 eV, respectively. According to the listed results in Table S5, the increasing trend of the electrochemical band gap for the investigated thin films in the order of LNO-TF/ED-V1 > LNO-TF/ED-V2 > LNO-TF/ED-V3 > LNO-TF/ED-T2 > LNO-TF/SG/P3HT:PCBM was well matched with the rising trend of the optical band gap. Since the optical and electrochemical band gaps were calculated using different equations and approaches, the optical band gap values for the LNO samples were greater. Moving from the LNO-TF/SG to the LNO-TF/ED-V1 sample,  $E_{ox}$  rose slightly from 0.68 to 0.73 V, increasing the  $E_v$  of the samples. The  $E_{red}$  values found for LNO-TF/SG (−1.34 V) and LNO-TF/ED-V2 (−1.65 V) were the highest and lowest among all samples, respectively.

Figure 10b–f illustrate band alignment schematics of the manufactured PSCs, which were generated using data obtained from the CV response of the samples. The ease of hole transfer at the interface of layers is influenced by the proximity of the  $E_v$  level of the LNO and the HOMO energy level of the active

layer. A smaller energy difference between these levels indicates a higher probability of hole transfer. The energy level proximity between the LNO and P3HT:PCBM layers increases the density of active sites for charge transfer and accelerates the rate at which holes can pass from the LNO to the P3HT:PCBM.<sup>16</sup> Based on the energy level calculations provided in Table S5, it was determined that the  $E_v$  level of LNO-TF/ED-V1 was approximately −5.13 eV. This was higher than the value acquired for the LNO-TF/ED-V2 sample (5.05 eV), LNO-TF/ED-V3 sample (5.03 eV), LNO-TF/SG sample (5.08 eV), and LNO-TF/ED-T2 sample (5.11 eV). According to Figure 10b, the  $E_v$  level of the LNO-TF/ED-V1 sample was −5.13 eV, which closely matches the HOMO energy level of P3HT (−5.30 eV). This observation implies that the LNO employed in this sample may be capable of facilitating hole transfer in a more efficient manner. Moreover, the increased  $E_c$  level of all the samples, particularly the LNO-TF/ED-V1 sample, compared to the P3HT LUMO energy level, contributed to the enhancement of their electron barrier capabilities.<sup>20</sup> Consequently, the PSCs fabricated with the LNO-TF/ED-V1 sample as the HTL exhibited superior photovoltaic performance to the PSCs prepared with other samples in this study.

This study involved the preparation of various thin films of LNO using both the ED and sol–gel methods, which were then employed as the hole transport layer (HTL) in PSCs. In Table 2, the photovoltaic characteristics of the developed PSCs are compared to those of some other binary and ternary metal oxides employed as the HTL in P3HT:PCBM-based BHJ PSCs reported elsewhere. As can be seen, the performance of the PSCs has been greatly influenced by the employment of the same metal oxide but prepared by different procedures. As indicated, the performance of PSCs can be altered by utilizing various techniques such as spin coating, thermal evaporation, and ED to prepare a thin film of NiO and V<sub>2</sub>O<sub>5</sub> as the HTL of P3HT:PCBM-based PSCs. Among different investigated methods, the ED method was found to produce the highest efficiency for indicated metal oxides. Similarly, the deposition technique for Cu<sub>2</sub>O and MoO<sub>3</sub> as the HTL in PSCs has also influenced their performance. Several studies have indicated that, compared to other techniques, spin-coating is the most effective method for enhancing the performance of PSCs utilizing Cu<sub>2</sub>O and MoO<sub>3</sub>. The fabricated BHJ PSCs in this study by employing electrodeposited LNO as the HTL exhibited superior photovoltaic performance compared to binary and ternary metal oxides previously utilized as HTL in

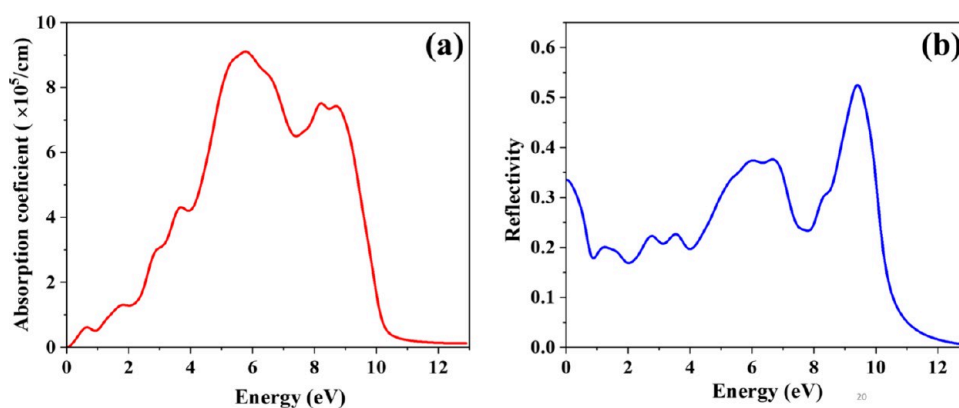


**Figure 11.** Calculated absorption coefficient (a) and reflectivity (b) spectrum for the rhombohedral LNO.

P3HT:PCBM-based PSCs. The aforementioned difference was pronounced in the case of the PSC-LNO-TF/ED-V1, which exhibited the highest photovoltaic performance among all the studied PSCs in this research. The PSCs based on the P3HT:PCBM active layer typically provide lower PCE than devices constructed by employing PM6 (PBDB-T-2F), PM7 (PBDB-T-2Cl), and D18 (PCE18) as donors and Y6 (BTP-4F) and Y7 (BTP-4Cl) polymers as nonfullerene acceptors (NFAs).<sup>55,56</sup> According to the results, it is anticipated that applying the highly efficient polymers mentioned above in the active layers of the PSCs produced in this study would considerably improve their photovoltaic performance.

### 3.8. Computational Results. 3.8.1. Optical Properties.

The optical features of the CTLs have a significant impact on the photovoltaic performance of PSCs. The optical characteristics of a material are directly impacted by its fundamental features. Thus, it is essential to comprehend how electromagnetic radiation interacts with materials, including absorption, transmission, reflection, and emission. Investigating the optical features of materials is a significant approach to interpreting their interaction with absorbed photon energy, which provides a predicted strategy for using the material in photovoltaic devices.<sup>66</sup>

The absorption coefficient  $\alpha(\omega)$  and reflectivity  $R(\omega)$  of the rhombohedral LNO crystal structure as two of the most significant and relevant optical features of CTLs in photovoltaic applications could be determined using the dielectric functions via eqs S10–S13 (Text S6). The plots of the overall spectra of both characteristics are presented in the energy range of 0–13 eV in Figure 11. The obtained results were greatly consistent with another study conducted about the optical properties of a rhombohedral LNO.<sup>36</sup> The inverse relation between the photon energy (in eV) and wavelength (in nm) could be expressed as  $E(\text{eV}) = \frac{1240}{\lambda(\text{nm})}$ .<sup>66</sup>

Light absorption is considered a limiting factor to applying a material as the HTL in conventional PSCs. It should be mentioned that the optical properties of a material in the visible region are more important than in the UV region for application as HTL in PSCs.<sup>67</sup> As exhibited in Figure 11a, the absorption coefficient  $\alpha(\omega)$  values for LNO began in the low-energy range and reached the highest value of  $9.1 \times 10^5 \text{ cm}^{-1}$  at 5.8 eV in the ultraviolet region ( $>5 \text{ eV}$ ). Moreover, absorption was negligible in the visible region (2–4 eV), indicating that this perovskite oxide is transparent enough and most of the light will pass through it, making LNO a good candidate for CTL in PSCs.

The reflectivity ( $R(\omega)$ ) is defined as the ratio of the energy of a reflected wave to the energy of the incident wave.<sup>68</sup> The reflectance behavior of photons at the surface of the studied material is depicted in Figure 11b. As can be seen, the static value of reflectivity at zero energy  $R(0)$  decreased for higher energies. The reflection of light was negligible, and most of the incident photons were transmitted in the visible region, confirming our earlier results for the absorption coefficient. The low  $R(\omega)$  and consequently the higher transmission of LNO emphasized its function as HTL in PSCs. The reflectivity of the studied perovskite oxide increased in the UV region, which revealed the reflection of a higher portion of the incident light in this area. The results obtained from the above-described optical calculations verified the potential function of the LNO as HTL for PSCs.

**3.8.2. Elastic properties.** The majority of research efforts in recent years have switched from focusing on increasing the efficiency to tackling the crucial problem of device stability.<sup>54</sup> The stability of solar cells is influenced by two main factors: (i) the active layer's relative humidity and thermal stability and (ii) the structural stability of the solar cell components, especially the electrodes, ETL, and HTL. Consequently, for high mechanical and thermal stability in PSCs, the CTLs should be stable under external variables such as high pressures and elevated temperatures.<sup>69</sup> The mechanical properties of a material are closely related to its elastic constant, making them a significant parameter of solids. Moreover, solid-state phenomena like brittleness, ductility, stiffness, and mechanical stability are closely connected to elastic constants.<sup>70</sup> Thus, mechanical and other important polycrystal features could be evaluated by determining single-crystal elastic constants. Based on the elastic calculations, which are explained in Text S7, LNO is a suitable material to be applied as the HTL of PSC to improve its mechanical flexibility and thermal stability.

## 4. CONCLUSIONS

Based on the most recent findings about the use of perovskite oxide thin films in third-generation solar cells, we came to the conclusion that the performance of bulk heterojunction polymer solar cells (BHJ PSC) could be improved using an electrodeposited  $\text{LaNiO}_3$  (LNO). Hence, the chronoamperometry electrodeposition (ED) process was successfully employed in synthesizing LNO nanostructures, where the deposition time (1, 2, and 4 min), potential magnitude (−1.09, −1.13, and −1.18 V), and electrolyte conditions (stirred/unstirred) significantly influence the structural and electro-

chemical characteristics of the electrodeposited LNO. First, the potentiostatic ED procedure was performed at three alternate deposition times of 1, 2, and 4 min by applying  $-1.18$  V. Then, at the optimal time of 2 min, the ED process was carried out under the same conditions, while the solution was gently stirred and compared with those samples obtained by applying  $-1.13$  and  $-1.09$  V in the stirred electrolyte. Subsequently, the physicochemical and electrochemical properties of prepared thin films were successfully characterized and compared with the sample prepared by the sol-gel process. Results indicated that applying the cathodic potential of  $-1.18$  V along with mild electrolyte stirring in 2 min led to the formation of more uniform and smaller LNO nanostructures possessing less surface roughness. Compared to all samples prepared in this work, employing the superior electrodeposited LNO sample as a hole-transporting layer (HTL) in the structure of BHJ PSC led to a short-circuit current density ( $J_{sc}$ ) of  $13.24$  ( $\text{mA cm}^{-2}$ ), open-circuit voltage ( $V_{oc}$ ) of  $0.64$  V, a high fill factor (FF) of 70%, an external quantum efficiency (EQE) of 75.3%, and the highest solar to energy conversion efficiency of 5.9%. This efficiency was approximately 73.5% greater than that obtained for the reference cell, which used the PEDOT:PSS as an HTL. Moreover, the PSC incorporating the best electrodeposited LNO sample exhibited remarkable ambient stability compared to other fabricated PSCs, maintaining 84% of its initial PCE after 450 h of aging. The enhanced device performance was ascribed to the uniform surface coverage, high electroactive surface area ( $1.341$   $\text{cm}^2$ ), high charge mobility ( $2.30 \times 10^{-6}$   $\text{cm}^2 \text{V}^{-1} \text{s}^{-1}$ ), enhanced surface contact area with the active layer, larger band gap resulting in the greater light absorption of the active layer, better energy level alignment, and lower charge recombination probabilities. The notable consistency observed between the DFT calculations and experimental results provided valuable information in understanding the structural, optical, and mechanical properties of this perovskite oxide, which could lead to the enhanced overall performance of PSC when employed as HTL in its structure.

## ■ ASSOCIATED CONTENT

### SI Supporting Information

The Supporting Information is available free of charge at <https://pubs.acs.org/doi/10.1021/acsaem.3c03274>.

Detailed information on the chemicals used, physico-chemical characterization, and electrochemical characterization of LNO nanostructures, computational methods, effects of potential magnitude in ED on LNO thin films, optical, and elastic properties of LNO nanostructures based on DFT calculations; naming details of LNO samples and fabricated PSCs, structural features of LNO rhombohedral crystal structure used in DFT, parameters extracted parameters from EIS measurements, obtained parameters from cyclic voltammograms and Tauc's plot, and calculated elastic constants; primitive cell of the LNO rhombohedral crystal structure, XRD patterns at  $800$  °C, EDS spectra, diameter distribution of LNO-TF/ED and LNO-TF/SG samples, SEM images, 3D AFM images, CV response, UV-vis spectra of LNO-TF/ED-V2, and LNO-TF/ED-V3 samples, 2D AFM images of the active layer coated LNO samples, and calculated surface contours of elastic modulus (PDF)

Optimized bulk structure of  $\text{LaNiO}_3$  (PDF)

Amount of energy with corresponding absorption coefficients and reflectivity (XLSX)

## ■ AUTHOR INFORMATION

### Corresponding Authors

Leila Naji – Department of Chemistry, AmirKabir University of Technology, Tehran 1591634311, Iran; [orcid.org/0000-0003-1593-2751](https://orcid.org/0000-0003-1593-2751); Email: [leilanaji@aut.ac.ir](mailto:leilanaji@aut.ac.ir)

Saeedeh Sarabadani Tafreshi – Department of Chemistry, AmirKabir University of Technology, Tehran 1591634311, Iran; School of Chemistry, University of Leeds, LS29JT Leeds, U.K.; [orcid.org/0000-0003-4130-437X](https://orcid.org/0000-0003-4130-437X); Email: [s.s.tafreshi@aut.ac.ir](mailto:s.s.tafreshi@aut.ac.ir), [S.SarabadaniTafreshi@leeds.ac.uk](mailto:S.SarabadaniTafreshi@leeds.ac.uk)

### Authors

Shirzad Jouybar – Department of Chemistry, AmirKabir University of Technology, Tehran 1591634311, Iran; [orcid.org/0009-0002-2664-7753](https://orcid.org/0009-0002-2664-7753)

Sayed Ahmad Mozaffari – Department of Chemical Technologies, Iranian Research Organization for Science and Technology (IROST), Tehran 3313193685, Iran; [orcid.org/0000-0002-6334-0294](https://orcid.org/0000-0002-6334-0294)

Nora H. de Leeuw – School of Chemistry, University of Leeds, LS29JT Leeds, U.K.; Department of Earth Sciences, Utrecht University, 3584 CB Utrecht, Netherlands; [orcid.org/0000-0002-8271-0545](https://orcid.org/0000-0002-8271-0545)

Complete contact information is available at: <https://pubs.acs.org/doi/10.1021/acsaem.3c03274>

### Notes

The authors declare no competing financial interest.

## ■ ACKNOWLEDGMENTS

The authors would like to gratefully thank the Research Affairs Division of the Amirkabir University of Technology (AUT), Tehran, Iran, for their financial support. This work is based on research funded by Iran National Science Foundation (INSF) under project no. 4002465. This work has used the computational facilities of the Advanced Research Computing at Cardiff (ARCCA) Division, Cardiff University, and HPC Wales. Via our membership of the UK's HEC Materials Chemistry Consortium, which is funded by EPSRC (EP/R029431), this work has also used the ARCHER2 UK National Supercomputing Service (<https://www.archer2.ac.uk>).

## ■ REFERENCES

- (1) Mamba, G.; Mafa, P.; Muthuraj, V.; Mashayekh-Salehi, A.; Royer, S.; Nkambule, T.; Rtimi, S. Heterogeneous advanced oxidation processes over stoichiometric  $\text{ABO}_3$  perovskite nanostructures. *Mater. Today Nano* **2022**, *18*, No. 100184.
- (2) Hong, Y.; Byeon, P.; Bak, J.; Heo, Y.; Kim, H.-S.; Bae, H. B.; Chung, S.-Y. Local-electrostatics-induced oxygen octahedral distortion in perovskite oxides and insight into the structure of Ruddlesden-Popper phases. *Nat. Commun.* **2021**, *12* (1), 5527.
- (3) Liu, D.; Zhou, P.; Bai, H.; Ai, H.; Du, X.; Chen, M.; Liu, D.; Ip, W. F.; Lo, K. H.; Kwok, C. T.; Chen, S.; Wang, S.; Xing, G.; Wang, X.; Pan, H. Development of perovskite oxide-based electrocatalysts for oxygen evolution reaction. *Small* **2021**, *17* (43), 2101605.
- (4) Chiabrera, F. M.; Yun, S.; Li, Y.; Dahm, R. T.; Zhang, H.; Kirchert, C. K. R.; Christensen, D. V.; Trier, F.; Jespersen, T. S.; Pryds, N. Freestanding perovskite oxide films: Synthesis, challenges, and properties. *Ann. Phys.* **2022**, *534* (9), 2200084.

- (5) Oliveira, L. C. C. B.; Venâncio, R.; de Azevedo, P. V. F.; Anchieta, C. G.; Nepel, T. C. M.; Rodella, C. B.; Zanin, H.; Doubek, G. Reviewing perovskite oxide sites influence on electrocatalytic reactions for high energy density devices. *J. Energy Chem.* **2023**, *81*, 1–19.
- (6) Mahmoudi, F.; Saravanakumar, K.; Maheskumar, V.; Njaramba, L. K.; Yoon, Y.; Park, C. M. Application of perovskite oxides and their composites for degrading organic pollutants from wastewater using advanced oxidation processes: Review of the recent progress. *J. Hazard. Mater.* **2022**, *436*, No. 129074.
- (7) Wang, H.; Zhou, M.; Choudhury, P.; Luo, H. Perovskite oxides as bifunctional oxygen electrocatalysts for oxygen evolution/reduction reactions—A mini review. *Appl. Mater. Today* **2019**, *16*, 56–71.
- (8) Wang, H.; Zhang, Q.; Qiu, M.; Hu, B. Synthesis and application of perovskite-based photocatalysts in environmental remediation: A review. *J. Mol. Liq.* **2021**, *334*, No. 116029.
- (9) Valadi, K.; Gharibi, S.; Taheri-Ledari, R.; Akin, S.; Maleki, A.; Shalan, A. E. Metal oxide electron transport materials for perovskite solar cells: a review. *Environ. Chem. Lett.* **2021**, *19* (3), 2185–2207.
- (10) Sheikh, M. S.; Roy, A.; Dutta, A.; Sundaram, S.; Mallick, T. K.; Sinha, T. Nanostructured perovskite oxides for dye-sensitized solar cells. *J. Phys. D: Appl. Phys.* **2021**, *54* (49), 493001.
- (11) Sorrentino, R.; Kozma, E.; Luzzati, S.; Po, R. Interlayers for non-fullerene based polymer solar cells: distinctive features and challenges. *Energy Environ. Sci.* **2021**, *14* (1), 180–223.
- (12) Kang, Q.; Liao, Q.; Xu, Y.; Xu, L.; Zu, Y.; Li, S.; Xu, B.; Hou, J. p-Doped conducting polyelectrolyte as an anode interlayer enables high efficiency for 1 cm<sup>2</sup> printed organic solar cells. *ACS Appl. Mater. Interfaces* **2019**, *11* (22), 20205–20213.
- (13) Kadam, K. D.; Kim, H.; Rehman, S.; Patil, H.; Aziz, J.; Dongale, T. D.; Khan, M. F.; Kim, D.-K. Compositional dynamics of the electron transport layer (ZnO: PEIE) in P3HT: PC61BM organic solar cells. *Mater. Sci. Semicond. Process.* **2021**, *136*, No. 106118.
- (14) Zeng, M.; Zhu, W.; Luo, J.; Song, N.; Li, Y.; Chen, Z.; Zhang, Y.; Wang, Z.; Liang, W.; Guo, B.; Zhang, K.; Huang, F.; Cao, Y. Highly Efficient Nonfullerene Organic Solar Cells with a Self-Doped Water-Soluble Neutral Polyaniline as Hole Transport Layer. *Sol. RRL* **2021**, *5* (3), 2000625.
- (15) Liu, J.; Shao, S.; Fang, G.; Meng, B.; Xie, Z.; Wang, L. High-efficiency inverted polymer solar cells with transparent and work-function tunable MoO<sub>3</sub>-Al composite film as cathode buffer layer. *Adv. Mater.* **2012**, *24* (20), 2774–2779.
- (16) Hasannezhad, F.; Naji, L.; Arvand, M. Comparative study of electrochemically-grown vanadium pentoxide nanostructures synthesized using differential pulse voltammetry, cyclic voltammetry, and chronoamperometry methods as the hole transport layer. *J. Alloys Compd.* **2022**, *900*, No. 163501.
- (17) Hosseinzade, M. R.; Naji, L.; Hasannezhad, F. Electrochemical deposition of NiO bunsenite nanostructures with different morphologies as the hole transport layer in polymer solar cells. *J. Electroanal. Chem.* **2022**, *926*, No. 116955.
- (18) Yin, Z.; Wei, J.; Zheng, Q. Interfacial materials for organic solar cells: recent advances and perspectives. *Adv. Sci.* **2016**, *3* (8), 1500362.
- (19) Shin, S. S.; Lee, S. J.; Seok, S. I. Exploring wide bandgap metal oxides for perovskite solar cells. *APL Mater.* **2019**, *7* (2), No. 022401.
- (20) Shang, Q.; Yu, J.; Hu, R.; Liu, Z.; Cheng, J.; Li, Y.; Shai, X.; Huo, M.-m.; Yang, X.; Li, L. Enhanced Charge Transport in Conventional Polymer Solar Cells with a Perovskite-Type LaNiO<sub>3</sub> Layer. *ACS Appl. Mater. Interfaces* **2020**, *12* (11), 13051–13060.
- (21) Wang, W.; Liu, Y.; Zhong, Y. J.; Wang, L.; Zhou, W.; Wang, S.; Tadó, M. O.; Shao, Z. Rational Design of LaNiO<sub>3</sub>/Carbon Composites as Outstanding Platinum-Free Photocathodes in Dye-Sensitized Solar Cells With Enhanced Catalysis for the Triiodide Reduction Reaction. *Sol. RRL* **2017**, *1* (7), 1700074.
- (22) Zhang, K.; Hu, Z.; Xu, R.; Jiang, X. F.; Yip, H. L.; Huang, F.; Cao, Y. High-Performance Polymer Solar Cells with Electrostatic Layer-by-Layer Self-Assembled Conjugated Polyelectrolytes as the Cathode Interlayer. *Adv. Mater.* **2015**, *27* (24), 3607–3613.
- (23) Al-Katrib, M.; Perrin, L.; Flandin, L.; Planes, E. Electrodeposition in Perovskite Solar Cells: A Critical Review, New Insights, and Promising Paths to Future Industrial Applications. *Adv. Mater. Technol.* **2023**, *8*, 2300964.
- (24) Atapattu, H.; De Silva, D.; Pathiratne, K.; Dharmadasa, I. Effect of stirring rate of electrolyte on properties of electrodeposited CdS layers. *J. Mater. Sci.: Mater. Electron.* **2016**, *27* (5), 5415–5421.
- (25) Zhang, Y.; Deng, J.; Mao, Q.; Jeong, S. Y.; Huang, X.; Zhang, L.; Lee, B.; Huang, B.; Woo, H. Y.; Yang, C.; Xu, J.; Wu, F.; Cao, Q.-Y.; Chen, L. Facilely Full-end-capping Engineering Promotes High-Performance Organic Solar Cells with Simultaneously Improved Efficiency and Stability. *Chem. Eng. J.* **2023**, *457*, No. 141343.
- (26) Yang, J.; Ding, W.-L.; Li, Q.-S.; Li, Z.-S. Theoretical Study of Non-Fullerene Acceptors Using End-Capped Groups with Different Electron-Withdrawing Abilities toward Efficient Organic Solar Cells. *J. Phys. Chem. Lett.* **2022**, *13* (3), 916–922.
- (27) Wheeler, G. P.; Choi, K.-S. Photoelectrochemical properties and stability of nanoporous p-type LaFeO<sub>3</sub> photoelectrodes prepared by electrodeposition. *ACS Energy Lett.* **2017**, *2* (10), 2378–2382.
- (28) Li, Y.; Yao, S.; Wen, W.; Xue, L.; Yan, Y. Sol–gel combustion synthesis and visible-light-driven photocatalytic property of perovskite LaNiO<sub>3</sub>. *J. Alloys Compd.* **2010**, *491* (1–2), 560–564.
- (29) Venugopal, M.; Kumar, H. P.; Satheesh, R.; Jayakrishnan, R. Effect of annealing temperature in the emission properties of nanocrystalline CaZrO<sub>3</sub>: 9SmxDy<sub>0.1–x</sub>O<sub>3</sub> systems prepared via self-propagating combustion synthesis. *Phys. Lett. A* **2020**, *384* (14), No. 126280.
- (30) Pierre, A. C. *Introduction to sol-gel processing*; Springer Nature, 2020.
- (31) Jouybar, S.; Yazdani, F. Synthesis of Magnetite Nanoparticles Under UV/IR Irradiation: Investigation of Effects on the Properties. *Nanosci. Nanotechnol. - Asia* **2018**, *8* (2), 289–296.
- (32) Bard, A. J.; Faulkner, L. R.; White, H. S. *Electrochemical methods: fundamentals and applications*; John Wiley & Sons, 2022.
- (33) Zhao, M.; Li, Y.; Liu, L.; Zhao, C.; Jiu, T.; Hu, M.; Xiao, X. Non-planar tetrathiafulvalene derivative modified hole transporting layer for efficient organic solar cells with improved fill factor. *Sol. Energy* **2021**, *224*, 883–888.
- (34) Swami, S. K.; Chaturvedi, N.; Kumar, A.; Kumar, V.; Garg, A.; Dutta, V. Spray deposited gallium doped zinc oxide (GZO) thin film as the electron transport layer in inverted organic solar cells. *Sol. Energy* **2022**, *231*, 458–463.
- (35) Moutinho, H. R.; Jiang, C.-S.; To, B.; Perkins, C.; Muller, M.; Al-Jassim, M. M.; Simpson, L. Adhesion mechanisms on solar glass: Effects of relative humidity, surface roughness, and particle shape and size. *Sol. Energy Mater. Sol. Cells* **2017**, *172*, 145–153.
- (36) Guan, L.; Liu, B.; Jin, L.; Guo, J.; Zhao, Q.; Wang, Y.; Fu, G. Electronic structure and optical properties of LaNiO<sub>3</sub>: First-principles calculations. *Solid State Commun.* **2010**, *150* (41–42), 2011–2014.
- (37) Jain, P.; Arun, P. Influence of grain size on the band-gap of annealed SnS thin films. *Thin Solid Films* **2013**, *548*, 241–246.
- (38) Rabeh, M. B.; Khedmi, N.; Fodha, M. A.; Kanzari, M. The Effect of Thickness on Optical Band Gap and N-type Conductivity of CuInS<sub>2</sub> Thin Films Annealed in Air Atmosphere. *Energy Procedia* **2014**, *44*, 52–60.
- (39) Ab Malek, S. N.; Mohd, Y. Effect of deposition potential on the structure, electrocatalytic activity and stability of Pt films for methanol oxidation. *Int. J. Electrochem. Sci.* **2017**, *12*, 1561–1571.
- (40) Zheng, L.; Ma, Y.; Chu, S.; Wang, S.; Qu, B.; Xiao, L.; Chen, Z.; Gong, Q.; Wu, Z.; Hou, X. Improved light absorption and charge transport for perovskite solar cells with rough interfaces by sequential deposition. *Nanoscale* **2014**, *6* (14), 8171–8176.
- (41) Zhang, H.; Li, Y.; Zhang, X.; Zhang, Y.; Zhou, H. Role of interface properties in organic solar cells: from substrate engineering to bulk-heterojunction interfacial morphology. *Mater. Chem. Front.* **2020**, *4* (10), 2863–2880.
- (42) Tan, Z. a.; Qian, D.; Zhang, W.; Li, L.; Ding, Y.; Xu, Q.; Wang, F.; Li, Y. Efficient and stable polymer solar cells with solution-

- processed molybdenum oxide interfacial layer. *J. Mater. Chem. A* **2013**, *1* (3), 657–664.
- (43) Zheng, Z.; Hu, Q.; Zhang, S.; Zhang, D.; Wang, J.; Xie, S.; Wang, R.; Qin, Y.; Li, W.; Hong, L.; et al. A Highly Efficient Non-Fullerene Organic Solar Cell with a Fill Factor over 0.80 Enabled by a Fine-Tuned Hole-Transporting Layer. *Adv. Mater.* **2018**, *30*, 1801801.
- (44) Chin, Y.-C.; Daboczi, M.; Henderson, C.; Luke, J.; Kim, J.-S. Suppressing PEDOT: PSS doping-induced interfacial recombination loss in perovskite solar cells. *ACS Energy Lett.* **2022**, *7* (2), 560–568.
- (45) Liu, X.; Du, X.; Wang, J.; Duan, C.; Tang, X.; Heumueller, T.; Liu, G.; Li, Y.; Wang, Z.; Wang, J.; Liu, F.; Li, N.; Brabec, C. J.; Huang, F.; Cao, Y. Efficient Organic Solar Cells with Extremely High Open-Circuit Voltages and Low Voltage Losses by Suppressing Nonradiative Recombination Losses. *Adv. Energy Mater.* **2018**, *8* (26), 1801699.
- (46) Ruankham, P.; Choopun, S.; Wongratanaphisan, D.; Sagawa, T. Influence of surface modification with D205 dye on charge dynamics of hybrid ZnO nanorods/polymer solar cells. *Integr. Ferroelectr.* **2016**, *175* (1), 113–119.
- (47) Foroozandeh, A.; Abdouss, M.; SalarAmoli, H.; Pourmadadi, M.; Yazdian, F. An electrochemical aptasensor based on g-C<sub>3</sub>N<sub>4</sub>/Fe<sub>3</sub>O<sub>4</sub>/PANI nanocomposite applying cancer antigen<sub>125</sub> biomarkers detection. *Process Biochem.* **2023**, *127*, 82–91.
- (48) Rahmanian, A.; Naji, L. Systematic study of influencing parameters on the in-situ electrochemical growth of three-dimensional graphene on carbon cloth for supercapacitor applications. *J. Energy Storage* **2022**, *49*, No. 104146.
- (49) Sharifi-Viand, A.; Mahjani, M.; Jafarian, M. Investigation of anomalous diffusion and multifractal dimensions in polypyrrole film. *J. Electroanal. Chem.* **2012**, *671*, 51–57.
- (50) Shibayama, N.; Zhang, Y.; Satake, T.; Sugiyama, M. Modelling of an equivalent circuit for Cu<sub>2</sub>ZnSnS<sub>4</sub> and Cu<sub>2</sub>ZnSnSe<sub>4</sub>-based thin film solar cells. *RSC Adv.* **2017**, *7* (41), 25347–25352.
- (51) Shaban, M.; Benganem, M.; Almohammed, A.; Rabia, M. Optimization of the active layer P3HT: PCBM for organic solar cell. *Coat.* **2021**, *11* (7), 863.
- (52) Xiang, W.; Liu, S.; Tress, W. Interfaces and interfacial layers in inorganic perovskite solar cells. *Angew. Chem., Int. Ed.* **2021**, *60* (51), 26440–26453.
- (53) Mousavi, S. L.; Jamali-Sheini, F.; Sabaean, M.; Yousefi, R. Correlation of Physical Features and the Photovoltaic Performance of P3HT: PCBM Solar Cells by Cu-Doped SnS Nanoparticles. *J. Phys. Chem. C* **2021**, *125* (29), 15841–15852.
- (54) Xu, Y.; Yuan, J.; Zhou, S.; Seifrid, M.; Ying, L.; Li, B.; Huang, F.; Bazan, G. C.; Ma, W. Ambient Processable and Stable All-Polymer Organic Solar Cells. *Adv. Funct. Mater.* **2019**, *29* (8), 1806747.
- (55) Chen, X.; Liao, C.; Deng, M.; Xu, X.; Yu, L.; Li, R.; Peng, Q. Improving the performance of PM6 donor polymer by random ternary copolymerization of BDD and DTBT segments. *Chem. Eng. J.* **2023**, *451*, No. 139046.
- (56) Wang, Z.; Tang, A.; Wang, H.; Guo, Q.; Guo, Q.; Sun, X.; Xiao, Z.; Ding, L.; Zhou, E. Organic photovoltaic cells offer ultrahigh VOC of ~1.2 V under AM 1.5 G light and a high efficiency of 21.2% under indoor light. *Chem. Eng. J.* **2023**, *451*, No. 139080.
- (57) Steirer, K. X.; Chesin, J. P.; Widjonarko, N. E.; Berry, J. J.; Miedaner, A.; Ginley, D. S.; Olson, D. C. Solution deposited NiO thin-films as hole transport layers in organic photovoltaics. *Org. Electron.* **2010**, *11* (8), 1414–1418.
- (58) Wang, Z. Y.; Lee, S.-H.; Kim, D.-H.; Kim, J.-H.; Park, J.-G. Effect of NiOx thin layer fabricated by oxygen-plasma treatment on polymer photovoltaic cell. *Sol. Energy Mater. Sol. Cells* **2010**, *94* (10), 1591–1596.
- (59) Shen, W.; Yang, C.; Bao, X.; Sun, L.; Wang, N.; Tang, J.; Chen, W.; Yang, R. Simple solution-processed CuOX as anode buffer layer for efficient organic solar cells. *Mater. Sci. Eng. B* **2015**, *200*, 1–8.
- (60) Zhang, J.; Wang, J.; Fu, Y.; Zhang, B.; Xie, Z. Sonochemistry-synthesized CuO nanoparticles as an anode interfacial material for efficient and stable polymer solar cells. *RSC Adv.* **2015**, *5* (36), 28786–28793.
- (61) Li, Y.; Yu, H.; Huang, X.; Wu, Z.; Chen, M. A simple synthesis method to prepare a molybdenum oxide hole-transporting layer for efficient polymer solar cells. *RSC Adv.* **2017**, *7* (13), 7890–7900.
- (62) Chaturvedi, N.; Swami, S. K.; Dutta, V. Electric field assisted spray deposited MoO<sub>3</sub> thin films as a hole transport layer for organic solar cells. *Sol. Energy* **2016**, *137*, 379–384.
- (63) Zilberberg, K.; Trost, S.; Schmidt, H.; Riedl, T. Solution processed vanadium pentoxide as charge extraction layer for organic solar cells. *Adv. Energy Mater.* **2011**, *1* (3), 377–381.
- (64) Wang, J.; Ibarra, V.; Barrera, D.; Xu, L.; Lee, Y.-J.; Hsu, J. W. Solution synthesized p-type copper gallium oxide nanoplates as hole transport layer for organic photovoltaic devices. *J. Phys. Chem. Lett.* **2015**, *6* (6), 1071–1075.
- (65) Wang, J.; Lee, Y.-J.; Hsu, J. W. Sub-10 nm copper chromium oxide nanocrystals as a solution processed p-type hole transport layer for organic photovoltaics. *J. Mater. Chem. C* **2016**, *4* (16), 3607–3613.
- (66) Absike, H.; Baaalla, N.; Attou, L.; Labrim, H.; Hartiti, B.; Ez-zahraouy, H. Theoretical investigations of structural, electronic, optical and thermoelectric properties of oxide halide perovskite ACoO<sub>3</sub> (A= Nd, Pr or La). *Solid State Commun.* **2022**, *345*, No. 114684.
- (67) Haque, S.; Alexandre, M.; Mendes, M. J.; Águas, H.; Fortunato, E.; Martins, R. Design of wave-optical structured substrates for ultrathin perovskite solar cells. *Appl. Mater. Today* **2020**, *20*, No. 100720.
- (68) Ali, M.; Rahaman, M. Variation of the physical properties of four transition metal oxides SrTMO<sub>3</sub> (TM= Rh, Ti, Mo, Zr) under pressure: An ab initio study. *J. Adv. Phys.* **2017**, *6* (2), 197–205.
- (69) Wang, J.; Liu, Y.; Chen, X.; Chen, C.; Chen, P.; Wang, Z.; Duan, Y. Functional metal oxides in perovskite solar cells. *ChemPhysChem* **2019**, *20* (20), 2580–2586.
- (70) Khandy, S. A.; Islam, L.; Gupta, D. C.; Khenata, R.; Laref, A.; Rubab, S. DFT understandings of structural properties, mechanical stability and thermodynamic properties of BaF<sub>2</sub>O<sub>3</sub> perovskite. *Mater. Res. Express* **2018**, *5* (10), 105702.